Rice University

Optical spectroscopy and imaging systems for gynecological cancers: from Ultraviolet-C (UVC) to the Mid-infrared

by

Benjamin Appiah

A THESIS SUBMITTED
IN PARTIAL FULFILLMENT OF THE
REQUIREMENTS FOR THE DEGREE

Doctor of Philosophy

APPROVED, THESIS COMMITTEE:

Rebekah Drezek, Professor Bioengineering,
Electrical & Computer Engineering
Thesis Committee Chair

Kevin Kelly, Associate Professor
Electrical and Computer Engineering

Robert M. Raphael, Associate Professor
Bioengineering

Genevera Allen, Assistant Professor
Statistics

Houston, Texas
January 2011

Abstract

Optical spectroscopy and imaging systems for gynecological cancers: from Ultraviolet-C (UVC) to the Mid-infrared

by

Benjamin Appiah

Optical spectroscopy and imaging has proving to be of diagnostic relevance in many organ sites. We use fluorescence and FTIR spectroscopy to study gynecological organ sites and develop classification algorithms for cancer diagnosis. Ovarian cancer is the deadliest gynecological cancer. The American Cancer Society reports that for the year 2010, there would be 21,880 new cases of ovarian cancer and 13,850 fatalities. This is partly due to the fact that current diagnostic and screening methods for the disease are not very accurate. In this study, we analyze the fluorescence spectra of excised normal and cancerous ovarian tissues at multiple excitation wavelengths. The data includes spectra obtained at the UVC wavelength 270nm and UVB wavelength 300nm. Excitation in the UVC has been especially understudied in spectroscopy for tissue diagnosis. We introduce the application of a novel SVM algorithm for the classification of fluorescence data. This SVM is trained subject to the Neyman Pearson (NP) criterion which allows for a decision rule that maximizes the detection specificity whilst constraining the sensitivity to a high value. This technique allows us to develop a binary classification algorithm that is not biased towards the larger group and this in turn leads to robust classifiers that are more

suitable for clinical applications. We obtained sensitivities and specificities greater than 90% for ovarian cancer diagnosis using this algorithm. Also, FTIR is used to analyze cervical tissues. Absorption of light in the mid-IR region by biomolecules show up as peaks in the FTIR spectra, and there is differential absorption in tissue depending on the histopathology. The spectroscopic analysis informed our choosing of a wavelength for the illumination source of a mid-IR microscope. We then present the design of an imaging system that employs the use of a mid-IR quantum cascade laser(QCL) which can potentially have clinical use in the future. Finally a reflectance based fiber endoscope imaging system is presented. Cellular imaging is demonstrated with this system that has the potential for use in optical biopsy.

Acknowledgements

I would like to thank my advisor, Dr. Rebekah Drezek for introducing me to the field of biophotonics and for her help throughout my time in her lab. My gratitude goes to Dr. Kevin Kelly for being a part of my committee and for being generous with his time, always willing to have discussions whenever I approached him. My thanks go to Dr. Robert Raphael for giving me important and insightful advice throughout the years and serving on my committee. I am grateful to Dr. Genevera Allen for valuable critique which has improved my thesis and for agreeing to be a committee member. I would like to thank Dr. Vengadesan Nammalvar for his invaluable help and advice, without which making it through graduate school would have been difficult. I would also like to thank Dr. Jiantang Sun for fruitful collaborations, Chenghao Shu for all the great discussions, Mark Davenport for collaborations on statistical analysis and my lab colleagues.

Dedication

To Faustina Dudaah and Joseph Appiah,

admirable folks.

Table of Contents

List of Figures

List of Tables

Chapter 1: Introduction

1.1 Motivation

Gynecological cancers affect the organs and tissue of the female reproductive system. Among these, ovarian cancer is the most lethal having the highest mortality rate. Unlike other cancer types, very little is known about ovarian precancerous lesions and this contributes to the majority of ovarian cancer cases being diagnosed in the late stages. Cervical cancer on the other hand has well known precancerous lesions and the introduction of the Pap smear procedure has drastically decreased the mortality rate of the disease. It is nonetheless the second most common cancer affecting women. The definitive diagnosis for any gynecological cancer involves biopsy, a surgical procedure followed by microscopic examination. Fluorescence spectroscopy and imaging techniques have proven to be effective methods for tissue diagnosis and some spectroscopy systems have gained Food and Drug Agency (FDA) approval for use as adjunctive methods in the diagnosis of cancer. These systems use classification algorithms for automated diagnosis of the disease while biopsy and subsequent examination is a subjective process dependent on the skill of the examiner. A review of the literature indicates that in the training of classification algorithms, the size of the control group (normal) is usually larger, and in many cases much larger than the size of the malignant (cancer) group. Such algorithms may be prone to skewed classification results since they train for a decision rule that maximizes overall classification accuracy. Obviously well tailored algorithms that avoid this problem would no doubt make the systems already on the market or that are being evaluated function better. We present the

application of a classification algorithm that can help prevent the skewed classification problem.

Moreover current fluorescent spectroscopic systems are in need of improvement in their diagnostic accuracy. We present the classification results of spectroscopic data excited at the UVC wavelength of 270nm and show that it is a diagnostically significant wavelength in ovarian tissue diagnosis. The UVC wavelength region has been neglected due to concerns about tissue mutagenicity, but a number of studies support the fact that low power levels of excitation are safe. Incorporating UVC excitation wavelengths in current systems may lead to better classification results.

The strong light absorption of tissues in the Mid-infrared (mid-IR) makes it challenging for optical systems operating in this wavelength region to be used for diagnosis. But many molecules have their vibrational modes excited in this wavelength region. Many of these molecules are tissue constituents and they exhibit distinct absorption peaks throughout the mid-IR region. We study the Fourier transform infrared (FTIR) absorption spectra of cervical tissue samples and after noting diagnostically significant wavelengths, we proceed to assemble a reflectance based mid-IR imaging system that use a high brightness quantum cascade laser (QCL) as an illumination source. Our hope is that in the future, optimized versions of such systems may help in the evaluation and diagnosis of tissues.

Also the use of fiber probes for endoscopy holds promise for *in vivo* diagnosis in a lot of tissue sites that may be difficult to access non-invasively. We develop a reflectance-mode fiber microendoscope (RFM) system that is low cost and may have

potential for cancer diagnosis in the future. The algorithms, spectroscopy and imaging systems we have developed hold a lot of promise for aiding in the diagnosis of gynecological cancers.

1.2 Specific Aims

The goal is to develop algorithms and optical systems that would be useful as stand alone or adjunctive methods for the diagnosis of gynecological cancers and cancer in other organs as well. The specific aims for this thesis are:

1. To demonstrate the application of a Neyman Pearson (NP) SVM algorithm that yields balanced classification results for discriminating ovarian cancer spectra from that of other tissue types regardless of the relative group size.
2. To demonstrate the diagnostic potential of UVC excitation fluorescence.
3. To develop a reflectance-mode fiber microscope (RFM) for possible endoscopic or biopsy applications.
4. To study FTIR mid-IR absorption spectra of formalin-fixed cervical tissues and to develop classification algorithms for discriminating between spectra of cervical cancerous and normal tissues.
5. To present work on the development of a reflectance mode QCL microscopy system.

1.3 Dissertation Overview

Chapter 1 gives a short overview of optical spectroscopy, fiber probes for Ultraviolet-visible (UV-Vis) endoscopic imaging, ovarian and cervical cancer. Chapter 2 presents measurement of the ovarian fluorescence spectra. Chapter 3 presents work on fluorescence spectroscopy and classification of ovarian tissues. The learning method of Support Vector Machines (SVM) is introduced and the Neyman Pearson(NP) training of ovarian fluorescence spectra for cancer diagnosis is presented. Chapter 4 presents the development and applications of the reflectance-mode fiber microscope. Chapter 5 presents the classification algorithms for the diagnosis of FTIR cervical spectra, discriminating between cancerous and normal tissues. Chapter 6 presents the development of the QCL based Mid-IR imaging system. Chapter 7 summarizes the thesis.

1.4 Optical Spectroscopy

Optical Spectroscopy deals with extracting information from the interaction between light and biological tissue. The information spectroscopy affords us include biochemical morphological properties of the tissue under interrogation. These properties change with the progression of tissues from normal to cancer, hence by using spectroscopy to access these properties we uncover information that can guide us in determining tissue histopathology. Some of the common spectroscopic modalities include fluorescence, diffuse reflectance, Fourier transform infrared spectroscopy (FTIR) and Raman spectroscopy. Each of the modalities provides some information about the tissue that may be exploited for differentiating between different tissues types or for diagnostic

purposes. For example diffuse reflectance provides information about absorption and scattering properties which have been observed to be different for diseased and normal tissues and light scattering spectroscopy gives us information about nuclear size distribution in the epithelial layer, a property which has been observed to be a feature of precancerous and cancerous changes.

In this thesis, we used FTIR and fluorescence spectroscopy to develop classification algorithms for cervical and ovarian tissues respectively. The mechanism of fluorescence involves the excitation of a molecule (in the UV-Vis) into a higher energy level and its eventual relaxation to the ground state, accompanied by the emission of photons of a longer wavelength. The information accessed with fluorescence spectroscopy includes tissue biochemistry and the concentration of these biomolecules. FTIR involves the use of a broadband light source and a Michelson interferometer, to collect an interferogram of the tissue and then converts the interferogram to a spectrum by a Fourier transform algorithm. The information we can access in tissues is the distinct molecular vibrations which get excited at specific wavelengths in the mid-IR. Differences in the functional groups of molecules of cancerous and normal tissues can be utilized for classification purposes.

1.5 Survey of Fiber Optics Imaging and Endoscopy in the UV-Vis

Typically, fiber-optic imaging or endoscopic systems operating in the Ultraviolet-visible region (UV-Vis) use a fiber-optic cable for illumination and collection of light via a lens system. Conventional endoscopic applications often utilize a broadband light source for illumination of the sample. This has a limiting effect on the image contrast, as well as confines imaging to the surface of the sample eliminating the effective use in optical sectioning. The use of a filter to narrow the bandwidth of the source, usually selecting light in the blue region for illumination has been shown to improve image contrast.[1-3] Also fiber-scanning confocal microscopy is a technique that has shown a lot of promise. Confocal microscopy itself allows for the selective imaging of different layers of tissue. It does this by the use of point illumination and a pinhole to eliminate out-of-focus light in tissue specimens thicker than the focal plane. This is a significant advantage over conventional wide-field microscopy and even allows for three-dimensional imaging capability by scanning many thin sections. In the focal plane, all points from areas outside of the focal point are also blocked by the pinhole screen and this ensures enhanced lateral resolution. With the addition of a fiber probe and a simple lens system to a standard confocal microscope, a fiber-scanning confocal system can be realized. This system has great potential for *in vivo* imaging but requires a scanning system which sweeps through the fiber end, objective lens or specimen to record the images. Scanning mechanisms that have been used in fiber-optic imaging include piezoelectric driven tip tilt mirrors, piezoelectric actuators to facilitate compact scanning and miniaturized microelectromechanical systems (MEMS) scanning mirrors which can be as small as 0.5mm.[4-5]

Fluorescence imaging with fiber probes have been reported in a number of studies.[4,6] The fluorescence technique can increase contrast and enhance quality of images. Polglase *et al.* developed a confocal endomicroscope for the *in vivo* fluorescence imaging of the upper and lower GI tract. With the use of intravenously administered fluorescein and topically applied acriflavine, clear images including the nuclei of the GI tract were obtained.[7] A notable study involving the use of a fiber-optic confocal system for *in vivo* imaging of human skin has been reported by Swindle *et al.*[8] They reported the imaging of different layers of the skin and found detailed changes in skin morphology as deeper layers were imaged. For instance their findings included changes in keratinocyte size and shape with progressive imaging into deeper layers of the epidermis which suggest the ability of this technique to give valuable insight into depth-dependent tissue morphology. However, the use of exogenous fluorophores in the studies cited above pose the problem of possibly altering the tissue microenvironment which in turn makes it difficult to interpret the imaging results for disease detection.[9] Relying only on endogenous tissue fluorescence signals can sidestep the issues with exogenous agents. However, autofluorescence compared to exogenous fluorescence applications generally suffer from low intensity and also suboptimal specificity. Nevertheless significant autofluorescence work has been reported. Mayinger *et al.* used the technique to discriminate between normal and cancerous tissues of the esophagus by noting the higher intensity signal of the normal tissues.[10] A combination of fiber-optic autofluorescence and reflectance imaging was used to form composite images for the discrimination of early esophageal cancer tissues.[11]

Advances particularly in photonic crystal fiber technology has encouraged the extension of fiber optic imaging into applications involving two-photon imaging.[4,12-13] In this application, the use of photonic fibers ensure the delivery of femtosecond pulses with vastly reduced distortion, pulsed width broadening and modal interference. This has facilitated the design of a handheld miniaturized two-photon microscope which has been used for the imaging of diseased skin tissues.[13] An extremely compact fiber optic two-photon system using a multimode fiber collector has also been used to acquire quality fluorescent images of animal tissues.[14] Two photon systems have the advantage that they can be used in imaging at different layers of a tissue just like the confocal systems and even enjoy deeper penetration into tissues, but the femtosecond pulse lasers used for excitation are very expensive. Fiber probes have also been used with other optical techniques such as optical coherence tomography(OCT)[15], Raman[16] and FTIR[17], for studying biological tissues. Employing fiber-optic bundles for imaging instead of single fibers has also been considered. Fiber bundles are made of up to around 100,000 individual fibers in a tightly packed arrangement which is consistent throughout its length. This allows for the transmission of the image of samples in a pixilated form. Muldoon *et al.* reported the development of a low cost fiber-bundle microscope for the fluorescence imaging of Barrett's esophagus.[18] Their objective was to build a low cost system, and the components of the system added up to less than $2500. Subsequently a study involving *ex vivo* tissues was done and a quantitative image analysis algorithm using textural features was used to obtain a sensitivity of 87% and a specificity of 85% for identifying neoplastic lesions in the esophagus.[19]

In this thesis, the design and development of a high-resolution fiber bundle reflectance-mode (RFM) microendoscope is presented.[20] The endoscopic system has a resolution of around 3.5um and was designed for use in optical tissue biopsy. Also, it is low cost and can be easily converted for use in fluorescence imaging with minimal effort. Moreover the use of a fiber bundle eliminates the need for scanning as the light source was fully coupled into the bundle, cutting down on system complexity.

1.6 Gynecological Cancer

1.6.1 Ovarian Cancer

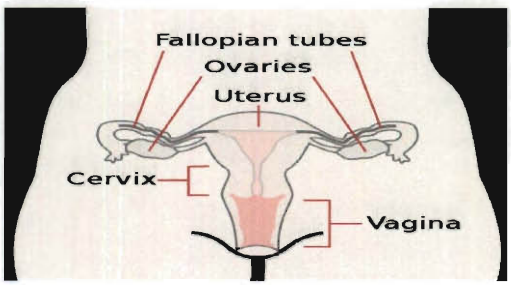

Figure 1.1- Anatomical image of the female reproductive system showing organs that are affected by gynecological cancer. Courtesy of the Centers for Disease Control and Prevention and from Reference 21.

Ovarian cancer has the highest mortality of all gynecological cancers. Overall, it is the fifth leading cause of all cancer deaths in women. The underlying biology of the disease is still being explored and currently not well understood. The most common type of the disease originates from the epithelium which accounts for about 85%-95% of the total. Rarer types can be found in the stroma of the ovary and the germ cell which is the egg producing cell of the organ. Other tissue abnormalities include benign tumors, which

is growth of abnormal cells that don't pose a risk of spreading to other sites, and cysts. It is estimated that only 20% of the disease is detected before tumor metastases. One of the main reasons is the lack of understanding of early symptoms of the disease. Figure 1.1 is an image of the female reproductive system showing the organs which are involved in gynecological cancers. It has recently been reported that ovarian epithelial tumors can be traced to the fallopian tubes and that this organ and not the ovary itself harbor the genesis of ovarian cancer.[22]

Until the consensus statement released in 2007 by the American Cancer Society (ACS) detailing common symptoms that suggest the onset of the disease, it was widely accepted that any early signs of the disease were imperceptible. The symptoms include bloating, frequent urination, abdominal pain and fullness. All these signs are nonspecific and could indicate a host of other ailments such as irritable bowel syndrome. Hence, a woman with ovarian cancer may be diagnosed with a different ailment before learning that she has cancer which may be too late for life saving treatment. Studies show that the awareness of these symptoms is of very limited value in the early detection of the disease. In a large study by Rossing *et al.*, involving 812 patients and 1313 control subjects, it was reported that the use of the symptoms detailed in the ACS consensus statement for ovarian cancer assessment is expected to result in the diagnosis of only 1 out of a 100 women with the symptoms in the general population.[23]

Some women are at a higher risk of developing the disease and would stand to benefit the most from accurate novel screening methods. The common risk factors include a family history of ovarian, breast or colon cancer, mutations in the BRCA1 and BRCA2 genes, age over fifty, exposure to talc and mutations in the p53 tumor suppressor

gene and the HER2 oncogene. Women who have had close relations (sister, mother or daughter) developed the disease are at risk. The BRCA1 and BRCA2 genes are tumor suppressors that in normal cells aid in stabilizing the cell's DNA and preventing uncontrolled cell growth. A harmful mutation in these genes put a woman at a huge risk of not only ovarian but breast cancer too. Lifetime risks for women in the general population is 14 out of 1000(1.4%) whilst that for those with the harmful BRCA1 or BRCA2 mutation is 150-400 out of 1000 for developing ovarian cancer (15-40%).[24] Most of the ovarian cancer cases are found in postmenopausal women, usually after 50 years old with more than half of the cases developing in women 65 years or older. Advances in technologies that provide information about genetic risk factors have been made. These include genetic testing for finding mutations in the BRCA1 and BRCA2 to determine a patient's risk of developing ovarian and breast cancers. The DNA chip technology is also available on the market for the detection of the p53 suppressor gene. Genetic testing, however, is expensive, takes a long time to get back results, and given the fact that it only gives information about the patients' risk of developing the disease, its usefulness is limited.

Screening methods for ovarian cancer include transvaginal ultrasound (TVU), the CA-125 antigen test and pelvic exams. TVU is an imaging method that involves the probing of the vaginal cavity with a transducer to look for abnormalities on the organ. This method is useful in detecting tumors but can't differentiate between benign masses such as cysts and cancerous tumors. The CA-125 antigen test involves investigation of the levels of the CA-125 protein in the blood. High levels of the protein correlate with a high risk of the disease, but in a lot of cases, women without the disease have high CA-

125 levels especially those in their child-bearing years, and some with average levels had already developed the disease. Furthermore, noncancerous diseases can increase CA-125 in blood. Pelvic exams involve the insertion of a speculum to open the vaginal walls and a physical inspection of the reproductive organs. None of these methods has an acceptable performance for screening according to a National Institute of Health (NIH) consensus statement, and furthermore there is no evidence suggesting that even the combination of all three methods provide acceptable sensitivity and specificity.

Positive significant impact in the cure of ovarian cancer lies in the development of better diagnostic tools than are currently available.[25] Hence our interest in investigating optical spectroscopic techniques particularly fluorescence spectroscopy and well tailored multivariate statistical analysis (MVA) for ovarian cancer diagnosis.

1.6.2 Cervical Cancer

It is estimated that by the end of 2010, the new cases for cervical cancer in the United States would climb to 12,200 and the fatalities from the disease would be at 4,210.[26] Worldwide estimates are staggering, with half a million women developing the disease and 250,000 women dying from it. The primary cause of the disease is the Human Papilloma Virus (HPV). It can be contracted through sexual contact and the different types of HPV number in excess of 100. Out of this number, about 15 are cancer-causing and 2 (HPV types 16 and 18) cause about 70% of the disease worldwide.[27] Still, only a small percentage of women with HPV infection would go on to develop cervical cancer. The cervix is pictured as part of the female reproductive system in Figure 1.1 above. With the introduction of the Pap smear procedure, the overall incidence and

mortality rate of the disease has dropped significantly reducing the mortality rate by 74% between 1992 and 1995. As the rate is still declining, it is the most successful cancer screening method in medical history. Yet the sensitivity of the Pap smear is very low[28,29] and a meta-analysis study found that it varies from 29%-56%.[30] Improvement on the technology using a thin layer based method for sample preparation called Thinprep™ has been approved by the FDA.[31] However, the additional expense that adopting this procedure would add to the cost of screening a patient is prohibitive and changes in the standard traditional procedure may not presently be warranted. During a Pap smear procedure, cells are taking from the cervix epithelium and examined under a light microscope to search for abnormalities that may indicate the presence of cervical precancer or cancer. An abnormal Pap smear, though, is usually the result of other factors beside the presence of cancer causing cells or HPV infection. These include vaginal infection, inflammation and other menopause related issues. When the result of a smear test is positive, a copolscopy, an examination of the cervix with a low powered microscope is usually done as a follow up to offer a complementary indication of disease presence. If the findings suggest abnormalities in the tissue, then a biopsy is performed to provide a more definitive diagnosis. A simple cervical biopsy referred to as punch biopsy involving the removal of a small tissue sample is the least invasive procedure. If warranted, a Loop Electrosurgical Excision Procedure (LEEP) which involves using a thin electrified wire operating at low voltage levels to remove tissue may be performed. Also if abnormalities are suspected inside the opening of the cervix, then endocervical biopsy involving the use of a curette to sample the organ is performed. And when severe abnormalities are detected, the more invasive cone biopsy is resorted to for removal of

tissues. This procedure entails the use of a scapel or carbondioxide laser to remove a cone-shaped sample of the tissue for further examination of cancerous cells. Irrespective of the effectiveness of the Pap smear, cervical cancer is the most common cancer, among women, besides that of the breast, and the most common of the gynecological cancers. New effective and cost-sensitive screening and diagnostic methods are needed if the estimated number of a quarter million worldwide fatalities is to be greatly affected. The diagnostic potential of optical detection methods make them good options to consider for the evaluation of cervical cancer.

[1]Chapter 2: Materials and Methods-Fluorescence Spectroscopy

2.1 Introduction

This chapter gives a description of the methodology used in the measurement of the fluorescence spectra of the ovarian tissue samples. Details including the spectral measurements retained for further analysis (analysis presented Chapter 3) and tissue handling protocol is given.

2.2 Measurements of EEMs of ovarian tissue

Patients undergoing exploratory laparotomy or transabdominal endoscopy and oophorectomy at the Arizona Health Science Center of the University of Arizona were participated in this *ex vivo* spectroscopy study. The study was reviewed and approved by the Institutional Review Boards of the University. A table top spectroscopy system was used to collect fluorescence data from ovarian tissue *ex vivo*. The spectroscopy system consisted of a scanning fluorometer with double excitation and emission spectrographs (Fluorolog 3-22, JY Horiba, Edison, NJ) equipped with a custom fiber optic probe which was coupled to the spectrographs with a fiber optic adapter positioned in the sample chamber. The probe interrogated a spot of 800μm diameter. Emission spectra ranging from 290nm to 700nm at excitation wavelengths in the range 270nm to 550nm were measured each from 49 patients. These were assembled into Excitation-Emission-Matrices (EEMs). An Excitation-Emission-Matrix (EEM) is a set of contour plots that show the intensity of tissues at various excitation and emission wavelengths. In this study, 3 excitation wavelengths of 270nm, 300nm and 340nm were used for further analysis. At

[1] This work is adapted from Reference 32.

the time of surgery biopsies, typically 5x10mm, were obtained from each ovary. Each biopsy was obtained from an area of interest selected by the surgeon. Corresponding ovary tissue was also taken for pathology. The tissue was rinsed with phosphate buffered saline (PBS) and placed on a biopsy tray under the fiber optic probe. The biopsies were placed in chilled RPMI culture medium (Mediatech Inc., Herndon, VA) to be transported to an optics laboratory for measurements. Each biopsy's fluorescence signal was collected at a sufficient amount of sites on the surface to cover the entire biopsy. The probe was positioned in contact with the surface epithelium. Each sample measurement took approximately 4 minutes and spectra were recorded from three or more locations on each biopsy. Optical signals were recorded within sixty minutes after removal. The system was calibrated with a set of positive and negative standards for purposes of wavelength and intensity calibration, as well as accurate background correction before every measurement. Deionized ultra filtered water served as negative standards, and positive standards were based on solutions of rhodamine, fluorescein and quinine. Data was reviewed by two experienced investigators. Samples were classified into four main groups: 1) Normal (no structures except stroma, epithelium corpus albicans and corpus luteum), 2) Benign neoplasm (abnormal growth without invasive areas), 3) Endometriosis (growth of endometrial glands and stroma on the ovary) or 4) Cancer (invasive carcinoma into the ovary). For this study the cancer and normal groups were chosen for more detailed analysis since too few samples fell into either of the other two groups. The Cancer group has 25 samples (fluorescence spectra measurements) and the Normal group has 180 samples. 8 measurements were classified as benign neoplasm and 10 were classified as endometriosis.

[1]Chapter 3: Support Vector Machine (SVM) via Neyman Pearson (NP) Classification of Ovarian Tissues

3.1 Introduction

Ovarian cancer is the deadliest gynecological cancer. The American Cancer Society estimates that for the year 2010, there would be 21,880 new cases of ovarian cancer and 13,850 deaths would result from the disease.[33] It ranks fifth as the cause of cancer death in women and a woman has a 1 in 72 lifetime risk of developing the disease.[34] Findings of the Surveillance, Epidemiology and End Results (SEER) Program of the National Cancer Institute suggest that the survival rate for ovarian cancer hasn't improved in 30 years since the 'war on cancer' was declared, whilst cancer affecting other again sites has significantly decreased mortality rates.[33,34] Ovarian cancer is relatively hard to detect because currently there is no sound understanding of any preinvasive lesions. However, detection of the disease can be greatly improved by low cost technologies that can automate the diagnostic process and also increase the diagnostic accuracy. Fluorescence spectroscopy offers this opportunity. Moreover, the technique can relate tissue biochemistry and morphological properties to the spectrum.

A large body of work has demonstrated that tissue classification based on fluorescence spectroscopy can be used for the diagnosis of cancerous tissues. It has been used extensively for the diagnosis or classification of cervical tissue dysplasia.[35-38] Gupta *et al.* obtained specificity and sensitivity, each greater than 99% for the *in vitro*

[1] This work is adapted from Reference 32.

discrimination between cancerous and benign/normal breast tissues.[39] Scwharz *et al.* used the technique to diagnose oral cancer and dysplasia *in vivo*. The study involved both keratinized and non-keratizined tissues and they reported a sensitivity of 82% and a specificity of 87% for a relatively large independent validation set of 119 sites.[40] Yang *et al.* found that in colon tissues, discrimination between adenocarcinoma and normal tissues yielded accuracy above 90% using intensity ratios involving excitation and emission wavelengths.[41] In a study involving wavelengths from the UVA and UVB regions by Wang *et al.*, an algorithm using the ratio of integrated fluorescence intensities was used to distinguish *ex vivo* cancerous colorectal tissues from benign ones.[42] Zaak *et al.* used an excimer laser operating at 308nm to probe bladder tissues of patients undergoing transurethral resection. They could diagnose bladder cancer with a sensitivity of 95% and specificity of 77%.[43]

Approaches to tissue optical spectra classification usually falls into two main groups: the model-based approach and the empirical approach. The model based approach, which provides a direct quantitative basis of the contributions of different tissue chromophores to a spectrum, uses biological and optical parameters extracted from physically-based models as features in classification algorithms. More recently, Redden-Webber *et al.* implemented physically-based models for both reflectance and fluorescence spectroscopy of the cervix and analyzed the data of 330 patients.[44] The combination of the two modalities into an adjoint algorithm yielded a sensitivity and specificity of 85% and 51% respectively. Studies have especially been done on tissue classification using monte carlo models. For example, a monte carlo inverse model of diffuse reflectance was employed to classify the spectra of freshly excised breast tissues

into malignant or non-malignant groups. The classification was based on extracted features including hemoglobin saturation, total hemoglobin concentration, beta-carotene concentration and the reduced scattering coefficient.[45] The empirical approach involves algorithms based on features directly selected from the raw spectrum or some transformation of the original data. A review of the literature suggests that in general, the latter produces better classification results than the former. Both approaches, but especially the empirical, rely heavily on the use of multivariate statistical analysis (MVA) methods. The most widely used methods for analysis or classification in tissue spectroscopy include Linear Discriminant Analysis(LDA),[46,47] Artificial Neural Network(ANN)[48] and K-Nearest Neighbors(kNN).[49,50] Chandra *et al.* analyzed the measured fluorescence and reflectance spectra from pancreatic tissue and implemented an LDA algorithm based on the two modalities. Tissue fluorescence was excited at 355nm and the algorithm yielded a sensitivity of 85% and a specificity of 89% with negative and positive predictive values of 92% and 80% respectively.[51] Nayak *et al.* used ANN for classification involving oral malignancies.[52] Features were extracted from emission spectra obtained at 325nm of pulsed laser excitation and then fed into the algorithm to obtain a specificity and sensitivity of 100% and 96.5% respectively. Kamath *et al.* used a kNN based algorithm for differentiating, with high accuracy, colonic mucosal tissue fluorescence of a normal group from one comprised of malignant tissues.[50]

Analysis of ovarian tissue fluorescence spectra is scant in the literature, compared to that of the other organs cited above. Utzinger *et al.* has done exploratory studies to differentiate between the reflectance spectra of different ovarian tissue types, [53] and Brewer *et al.* has explored fluorescence spectroscopy and microscopy of the ovary.[54,55]

Kamath *et al.* used fluorescence excitation at the single wavelength of 325nm, and MVA to distinguish the spectra of ovarian tissues,[49] and more recently Tanbakucki *et al.* developed a confocal microlaparoscope designed for real-time imaging of the ovarian epithelium.[56] Also, the use of wavelengths below 300nm for the excitation of tissue fluorescence is relatively uncommon despite studies showing that it is safe at low excitation power.

In this study, we analyze the fluorescence spectra of excised normal and cancerous ovarian tissues at multiple excitation wavelengths and use the spectral data for binary classification. The data includes spectra obtained at the UVC wavelength of 270nm, the UVB wavelength of 300nm and at 340nm, an often useful diagnostic wavelength. The first wavelength has been rarely examined for diagnostic significance. We used both the sensitivity/specificity/accuracy metric and the Area Under Curve (AUC) to assess diagnostic performance rather than just relying on one metric. We obtained comparable classification results for all of the 3 excitation wavelengths for discrimination between cancer and normal tissues (cancer vs. normal) and for discrimination between cancer and noncancerous tissues (cancer vs. noncancer). We introduce the application of a novel SVM algorithm for binary classification of fluorescence data. This SVM is trained subject to the Neyman-Pearson (NP) criterion, in which we find a decision rule that maximizes the specificity while constraining the sensitivity to be a high value. Traditional learning approaches involve seeking a decision that maximizes the overall accuracy rather than either the sensitivity or specificity. By modulating the threshold, we can selectively train for either high specificity or sensitivity values rather than the overall accuracy. This flexibility in algorithm development makes it attractive as an adjunct

modality to already existing screening methods such as the conventional ultrasound which routinely yields low positive predictive values for the screening of ovarian cancer. Also this learning approach may be able to improve the performance of currently available optical spectroscopic diagnostic tools on the market. Moreover, this algorithm is especially suitable for dealing with unbalanced data involving one group having a far larger size than the other. Unbalanced data has a tendency of biasing an algorithm's performance towards the group with the larger size. Zhu *et al.* underscored this problem in their breast tissue fluorescence study, in which an SVM was used in classification involving 27 malignant and 94 nonmalignant tissue samples.[57] They concluded that the lower sensitivity compared to the specificity their SVM algorithm yielded, was likely due to the unbalanced data set. A review of the literature suggests that it is very common for studies to have unbalanced data set in which the control/normal group has a relatively larger size or a far larger size than the disease group. The data in this study is no exception with 25 members in the cancer group versus 180 in the normal group and 198 in the noncancer group. This algorithm that trains data subject to the NP criterion, may be more suitable than traditional ones in the training and classification of unbalanced datasets. Also, we analyze the data with dimension reduction methods principal component analysis (PCA) and partial least squares (PLS) and use PLS to reduce the feature size required for training.

3.2 SVM in Optical Spectroscopy

Algorithms based on SVM have been successfully used for the classification of optical spectroscopic and other types of medical data.[57-60] In the field of fluorescence spectroscopy, a study employed a linear kernel SVM in grouping breast tissues into malignant and nonmalignant groups.[58] The SVM inputs were based on features extracted from a montecarlo model of fluorescence and diffused reflectance. Different combinations of the extracted parameters including hemoglobin saturation, reduced scattering coefficient, and the relative concentration of individual flourophores were used as inputs into the SVM algorithm to yield different classifiers, some of which produced classification accuracies of greater than 86%. Palmer *et al.* used a similar montecarlo model to extract features for an SVM algorithm that yielded a sensitivity and specificity of 82% and 92%, respectively.[59] Only two features, the hemoglobin saturation and the reduced scattering coefficient were used as input parameters and the dataset involved 17 histopathologicaly malignant and 24 normal/benign *ex vivo* breast tissues. In a study by Majumder *et al.*, a recursive feature selection was integrated into an SVM algorithm, for the purpose of reducing the dimension of the feature space, to train oral spectroscopic data. This integrated algorithm was tested on an independent data set to yield a sensitivity and specificity of 93% and 97% respectively.[60] They noted that this outperformed a Fisher's Linear Discriminant algorithm tested on the same data. Further studies have confirmed the superiority of SVM over algorithms in learning data. For the classification of PET brain images, an SVM improved on the performance of a neural network(NN) yielding an error rate of 7.1% compared to 14.3% for the NN.[61]

3.3 Algorithm

3.3.1 General Binary Classification

In binary classification algorithms, a general rule from an input data sample that also holds true for new data is sought. The given data can be formalized as S = $\{(\boldsymbol{x_i}, \boldsymbol{y_i}) \mid \boldsymbol{x_i} \in \mathbb{R}^{\boldsymbol{p}}, \boldsymbol{y_i} \in \{-\mathbf{1}, +\mathbf{1}\}\}^{\mathrm{n}}$, $\boldsymbol{x_i}$, the feature vector, is a vector of the data points for the *i*-th data sample, for example in the case of discrimination using the spectral data, it corresponds to the intensity values that make up the fluorescence emission spectrum. p is the feature size, n is the total sample size and $\boldsymbol{y_i}$ is the data label that can assume either of two values +1 or −1. The aim is to find a function f: $\mathbb{R}^{\boldsymbol{p}} \rightarrow \{-\mathbf{1}, +\mathbf{1}\}$ that predicts accurately the label of any new input data sample (feature vector). For example, in the case for classification of input data into cancer and normal groups, we use $\boldsymbol{y_i} \in -\mathbf{1}$ for any sample data belonging to the normal (control group) and $\boldsymbol{y_i} \in +\mathbf{1}$ is for samples belonging to the cancer group. The sensitivity, specificity and accuracy used for evaluating the binary classifier are defined as follow:

$$Sensitivity = \frac{TP}{P} = \frac{TP}{TP + FN}$$

$$Specificity = \frac{TN}{N} = \frac{TN}{TN + FP}$$

$$Accuracy = \frac{TP + TN}{P + N}$$

TP or true positive is the number of positive samples correctly classified; TN or true negative is the number of negative samples correctly classified; FP or false positive is the number of negative samples that are misclassified as positive; FN is the number of positive samples that are misclassified as negative; P denotes the total number of positive samples; N denotes the total number of negative samples.

3.3.2 SVM Formulation

SVM classification involves the mapping of the original input data, $\boldsymbol{x_i}$ into a higher dimensional feature space, $\boldsymbol{H}$, by the transformation $\boldsymbol{\Phi}: \mathbb{R}^p \rightarrow \boldsymbol{H}$, and then constructing a maximum margin hyperplane to separate the data into 2 classes (groups). The formulation, as detailed later in this section, involves the inner products of the vectors in feature space. But in using kernel functions $\boldsymbol{k(x_i, x_j)}$, with $\boldsymbol{k(x_i, x_j)} = \langle \boldsymbol{\Phi(x_i)}, \boldsymbol{\Phi(x_j)} \rangle$, we can actually sidestep the explicit evaluation of the mapping $\boldsymbol{\Phi}: \mathbb{R}^p \rightarrow \boldsymbol{H}$ and still evaluate the inner products. Partitioning of the data should be easier even allowing for the linear separation of data that would be linearly inseparable in $\mathbb{R}^p$.

$\boldsymbol{\Phi(x_i)}$	$\boldsymbol{k(x_i, x_j)}$
Polynomial of degree *d*	$\boldsymbol{(x_i . x_j + b)^d}$
Radial basis function	$\boldsymbol{e^{\frac{(\|x_i - x_j\|^2)}{2\sigma^2}}}$
Sigmoid	$\boldsymbol{tanh(ax_i . x_j - b)}$

Table 3.1- list of widely used SVM kernel functions.

Some of the most widely used kernel functions are listed in Table 3.1 above. In this study we chose the widely used RBF kernel for classification. The decision boundary is a linear combination of supporting vectors which are simply a subset of the training vectors with the closest proximity to the boundary. The advantages of SVMs over other conventional classification methods include the ability to use different kernel functions, ability to provide a global optimal solution and very high generalization ability owing to its basis of interclass margin maximization. Also one only has to pick few model parameters making training easy and the final classifier is stable and gives reproducible results. Barring numerical issues if the same SVM model, with the same parameters is used to classify a particular dataset multiple times, the solution would be the same.

In the traditional SVM, the *C*-SVM, the maximum margin hyperplane solves the quadratic program statement:

(1) $$\min(w,b,\xi) \quad \frac{1}{2}\|w\|^2 + C\sum_{i=1}^{n}\xi_i$$

s.t $$y_i(k(w,x_i)+b) \geq 1-\xi_i \qquad for\ i = 1,\ldots\ldots n$$

$$\xi_i \geq 0 \qquad for\ i = 1,\ldots\ldots n$$

with $C \geq 0$ controlling overfitting

A large *C* implies a high penalty for misclassification, ξ is a slack variable and it allows for misclassification of some of the training data, which is critical for unseparable data. *C* controls the tradeoff between the slack variable and the size of the margin; w is the normal vector and *b* is the bias that describes the discriminating hyperplane. An equivalent formulation known as the *v*-SVM was introduced to further clarify the

meaning of the penalty parameter, C. In this formulation, C is replaced with the parameter, $\nu \in [0,1]$. This parameter is the upper bound on the fraction of support vectors and the lower bound on the fraction of margin errors. The primal problem for the ν-SVM is:

(2) $$\min(w,b,\boldsymbol{\xi},\boldsymbol{\rho}) \quad \frac{1}{2}\|\boldsymbol{w}\|^2 - \boldsymbol{\nu\rho} + \frac{1}{n}\sum_{i=1}^{n}\boldsymbol{\xi_i}$$

$$\text{s.t} \quad \boldsymbol{y_i(k(w,x_i)+b) \geq \rho - \xi_i} \qquad \boldsymbol{for\ i = 1, \ldots \ldots n}$$

$$\text{and} \quad \boldsymbol{\xi_i \geq 0} \qquad \boldsymbol{for\ i = 1, \ldots \ldots n}$$

$$\text{and} \quad \boldsymbol{\rho \geq 0}$$

During training, ν is user supplied and $\boldsymbol{\rho}$ is optimized. C in the primal formulation is also user supplied.

The C-SVM and its corresponding ν-SVM formulation however only allow for the same weights on either group and hence proves to be unsuitable for problems that have unbalanced datasets. For binary classification problems, data imbalance results when the group size is much greater in one group compared to the other. The incidence rate of ovarian cancer among women at 12.9 per 10000 women is low as is the incidence rate of many diseases. Designing and conducting a clinical study involving the fluorescence spectra of patients come at the expense of money and time. Ideally investigators would like to use as much of the collected data from as many of the patients as possible for training a diagnostic algorithm. It is inevitable that recruiting patients for control data is easier than for cancer data and that the total sample size used for training

the algorithm would be tilted towards the control data. For this study, we have 180 normal and 198 noncancer samples each versus 25 cancer samples.

Cost sensitive SVMs which allow for different weights to be given to different classes have been formulated. The 2*C*-SVM and 2*v*-SVM have been proposed as the cost sensitive extensions for the *C*-SVM and *v*-SVM respectively.

Let $\boldsymbol{I_+ = \{i: y_i = +1\}}$ and $\boldsymbol{I_- = \{i: y_i = -1\}}$ The 2*C*-SVM has primal formulation:

(3)

$$\min(w,b,\xi) \quad \frac{1}{2}\|\boldsymbol{w}\|^2 + \boldsymbol{C\gamma}\sum_{i\in I_+}\xi_i + \boldsymbol{C(1-\gamma)}\sum_{i\in I_-}\xi_i$$

$$\text{s.t} \quad \boldsymbol{y_i(k(w,x_i)+b) \geq 1-\xi_i} \qquad \boldsymbol{for\ i = 1, \ldots \ldots n}$$

$$\boldsymbol{\xi_i \geq 0} \qquad \boldsymbol{for\ i = 1, \ldots \ldots n}$$

and dual:

(4)

$$\min(\alpha) \quad \frac{1}{2}\sum_{i,j=1}^{n}\boldsymbol{\alpha_i\alpha_j y_i y_j k(x_i,x_j)} - \sum_{i=1}^{n}\boldsymbol{\alpha_i}$$

$$\text{s.t} \quad \boldsymbol{0 \leq \alpha_i \leq C\gamma} \qquad \boldsymbol{for\ i \in I_+}$$

$$\boldsymbol{0 \leq \alpha_i \leq C(1-\gamma)} \qquad \boldsymbol{for\ i \in I_-}$$

$$\boldsymbol{\sum_{i=1}^{n}\alpha_i y_i = 0}$$

Where *C*, as mentioned previously controls overfitting and $\boldsymbol{\gamma} \in [0,1]$ adjusts the tradeoff between the 2 error types and hence the sensitivity and specificity.

The 2*v*-SVM has primal formulation:

(5) $$\min(w,b,\boldsymbol{\xi},\boldsymbol{\rho}) \quad \frac{1}{2}\|\boldsymbol{w}\|^2 - \boldsymbol{\nu\rho} + \frac{\gamma}{n}\sum_{i\in I_+}\boldsymbol{\xi_i} + \frac{1-\gamma}{n}\sum_{i\in I_-}\boldsymbol{\xi_i}$$

s.t $$\boldsymbol{y_i(k(w,x_i)+b) \geq \rho - \xi_i} \qquad \boldsymbol{for\ i = 1, \ldots \ldots n}$$

and $$\boldsymbol{\xi_i \geq 0} \qquad \boldsymbol{for\ i = 1, \ldots \ldots n}$$

and $$\boldsymbol{\rho \geq 0}$$

and dual

(6) $$\min(\alpha) \quad \frac{1}{2}\sum_{i,j=1}^{n}\boldsymbol{\alpha_i\alpha_j y_i y_j k(x_i,x_j)}$$

s.t $$\boldsymbol{0 \leq \alpha_i \leq \frac{\gamma}{n}} \qquad \boldsymbol{for\ i \in I_+}$$

$$\boldsymbol{0 \leq \alpha_i \leq \frac{1-\gamma}{n}} \qquad \boldsymbol{for\ i \in I_-}$$

$$\boldsymbol{\sum_{i=1}^{n}\alpha_i y_i = 0,\ \sum_{i=1}^{n}\alpha_i \geq \nu}$$

where $\nu \in [0,1]$ controls overfitting and $\boldsymbol{\gamma \in [0,1]}$ is a parameter that allows for trade of between the two error types and hence permits the adjustment of the sensitivity and specificity values. Hence the SVM application for the diagnosis of fluorescence spectra detailed in this study has 3 main advantages over the use of traditional SVMs reported in the literature. The algorithm can account for difference in group size and this makes it more appropriate for use in screening or diagnosis, the Neyman Pearson criterion allows

for us to set a high sensitivity value while training to maximize the specificity, and the user specified parameter is bounded and hence renders the algorithm far less arbitrary since the beginning and end points don't have to be chosen subjectively.

3.3.3 Neyman Pearson (NP)

In our usage of the NP classification paradigm, the aim is to find a decision rule that maximizes the specificity whilst maintaining the constraint that the sensitivity be at least equal to a desired user specified significance level, $\boldsymbol{\alpha}$.

The NP criterion then in terms of specificity and sensitivity is:

$\boldsymbol{f_{\alpha}^{NP} = \underset{f:sensitivity(f)\geq\alpha}{\overset{arg}{\overset{max}{}}} specificity(f)}$. So the SVM classification was performed subject to the NP criterion stated above. And this allows us to set an acceptable limit to the sensitivity whilst seeking the maximum specificity. [62-64] Further details about the NP algorithm is in Davenport *et al.*[62] and Scott *et al.*[63] For the NP training, a grid search over parameters $(\boldsymbol{\nu_+, \nu_-, \sigma})$ for the SVM RBF kernel was performed. Leave-one-out cross validated estimates of $sensitivity(f)$ and $specificity(f)$ were calculated and the parameter combination that maximizes $specificity(f)$ subject to $sensitivity(f) \geq \boldsymbol{\alpha}$ was sought. The highest specificity on the receiver operating characteristic (ROC) curve which fulfilled the NP criterion and its corresponding sensitivity were selected as the representative specificity and sensitivity respectively and reported in Section 3.5. The Area Under Curve (AUC) is also reported. The SVM parameter space for training is: for the bandwidth parameter, $\boldsymbol{\sigma}$ could assume values of 100 logarithmic space points between $\boldsymbol{10^{-10}}$ and $\boldsymbol{10^{10}}$, and $(\boldsymbol{\nu_+, \nu_-}) \in \boldsymbol{[0,1] \times [0,1]}$. In this study we were interested in ensuring that the sensitivity is high and so we set the threshold accordingly and the

SVM training was subjected to the classifier, f_{α}^{NP}. We wanted to train for the correct classification of at least 22 out of the 25 cancer samples (sensitivity of 88%), using the spectral data as features, and hence α was set to a value of 0.88. This α value produced stable classification results. For the classification involving the PLS components, $\alpha = 0.8$ was desired. It provided good results that were also stable. We could also just as easily constrain the specificity to be above a desired value and train to maximize the sensitivity instead.

3.4 Analysis methods

3.4.1 Principal Component Analysis (PCA) and Partial Least Squares (PLS)

Principal component analysis is a technique that transforms a given dataset composed of possibly correlated variables into a smaller number of uncorrelated variables, the principal components (PCs), and can reveal underlying dynamics in the dataset. The transformed data is expressed as the component scores. The first PC accounts for as much variability as possible in the dataset, and each subsequent PC accounts for as much of the remaining variability as possible. Hence, the dataset can be described by the first few PCs while the higher order PCs are usually uninformative and are due to noise. It is a true eigenvalue method, a widely used technique for dimensional reduction and has been applied to fluorescence spectroscopic data in numerous studies.[49,50] Partial Least Squares (PLS), another widely used method in optical spectroscopy,[45,65,66] is a regression method for dimension reduction, which in the

transformation of the dataset also takes into consideration the response variable (labels). In this case unlike in PCA, the construction of the PLS components (also referred to as PLS-C in this chapter) is done in such a manner that there is high covariance between the spectral variables and the corresponding labels.[67] This limits the impact of large variations in the dataset that may nonetheless be irrelevant in the classification algorithm. Detailed description of the PLS regression process is found in Geladi *et al.*.[68] In this study, we used PLS to reduce the dimension of the fluorescence data matrix and utilized the transformed PLS scores for differentiating the spectra of cancer and normal tissues of the ovary. It was also applied for the discrimination between cancer and noncancer tissues. Some of the PCs from the PCA analysis were used to visualize the data in component space. Being an unsupervised method, we may be able to visualize the transformed data without an imposition of the labels. The main reason for our use of PLS is to obtain acceptable results with a smaller feature size.

3.4.2 Selection of Components

The PLS components (PLS-Cs) that contributed to 99% of the total variance were selected as inputs to the wilcoxon ranksum test. The test is a nonparametric hypothesis test for the assessment of two independent observation samples. The component selection process is similar to that of other spectroscopic studies.[45,66] The PLS-Cs that showed statistically significant differences between the two groups at the significance value of ($p < 0.05$) were then chosen as having diagnostic value and hence used as attributes in the SVM classification.

3.4.3 Cross-validation

The idea of cross-validation is employed in testing classifiers when there are not enough samples to divide the dataset into a training/calibration set and a testing set. The premise is that the predictive ability of a model formed on part of a data (training set) can be tested out by how well it predicts the remainder of the data.[69] The idea of cross-validation involves dividing a dataset into p subsets and using p -1 subsets to build a statistical model and testing this model on the left out subset. A total of p different models are built, each model excluding a unique subset (containing samples not included in training the model) to be tested. A commonly used method of cross-validation is the leave one out cross-validation procedure. This involves building the model on all but one of the samples and using the resultant model to test out only the left out sample. In other words, the left out subset just contains one sample. This procedure is a method for assessing a model's performance[70,71] and was used in the determination of the generalization error of the SVM classifier. The proportions of the classification showing true positive and true negative results were used to calculate the sensitivity and specificity respectively. The classification accuracy was calculated as the proportion of the entire dataset accurately classified into their true groups.

3.5 Results

The raw bulk fluorescence spectra of all the measurements (involving the cancer and normal groups) are plotted in Figure 3.1. In Figure 3.1(a), the emission spectra of the tissues at 270nm excitation is shown and the wavelength range retained for classification is 290-515nm (46 spectral variables). Figure 3.1(b) shows spectra measurements at 300nm excitation. The emission wavelength range of 320-570nm is retained for classification (51 variables). Figure 3.1(c) shows the spectra measurements at 340nm of excitation which had the wavelength range of 360-640nm retained for classification (57 variables). It is clear from the figures that there is considerable variation in the intensities of the measured signals. In some cases the intrapatient variations exceed the interpatient variations which underscore the need for spectra preprocessing. The preprocessing involved normalization of each measurement to its peak emission intensity. Preprocessed fluorescence spectroscopic data was used as input features for the SVM classification as depicted in Figure 3.2, the algorithm flowchart. The bulk fluorescence spectra is a data matrix consisting of the emission spectra for all the measurements in both classification groups for each excitation wavelength. The cancer group size was 25 and the normal group size was 180.

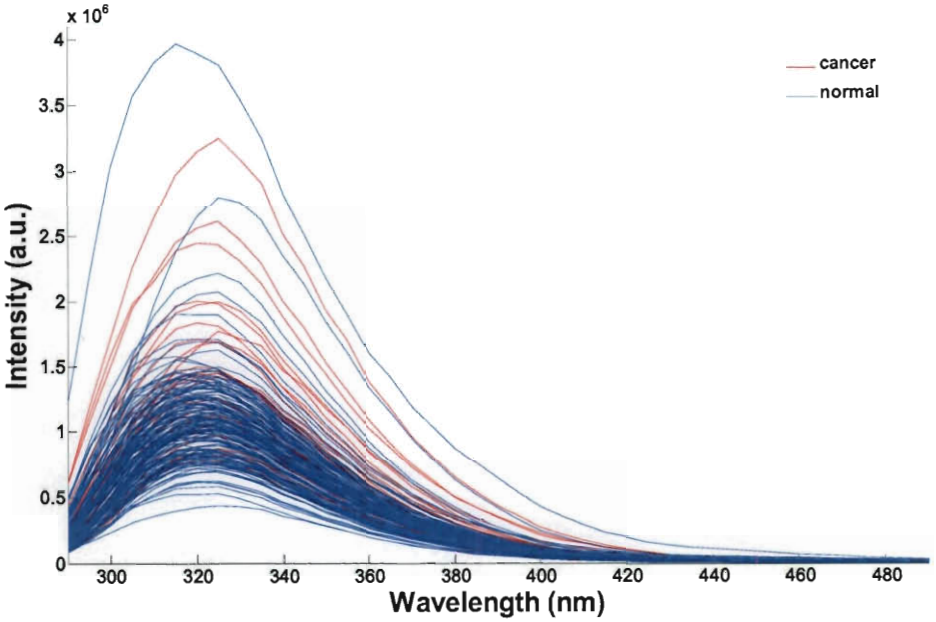
x 10^6
4
3.5
3
2.5
2
1.5
1
0.5
0
Intensity (a.u.)
300
320
340
360
380
400
420
440
460
480
Wavelength (nm)
cancer
normal

(a)

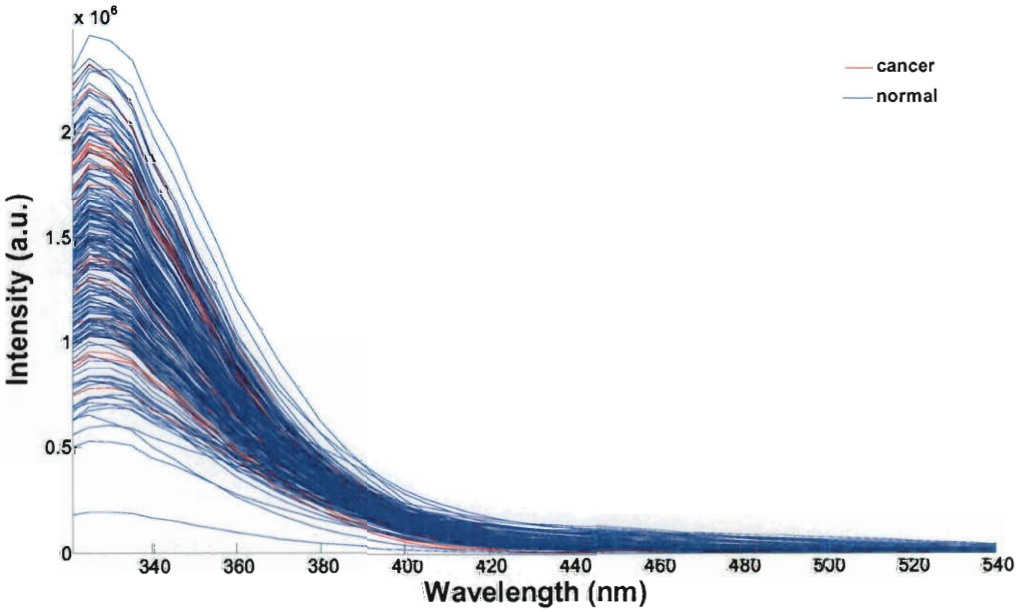
x 10^6
2
1.5
1
0.5
0
Intensity (a.u.)
340
360
380
400
420
440
460
480
500
520
540
Wavelength (nm)
cancer
normal

(b)

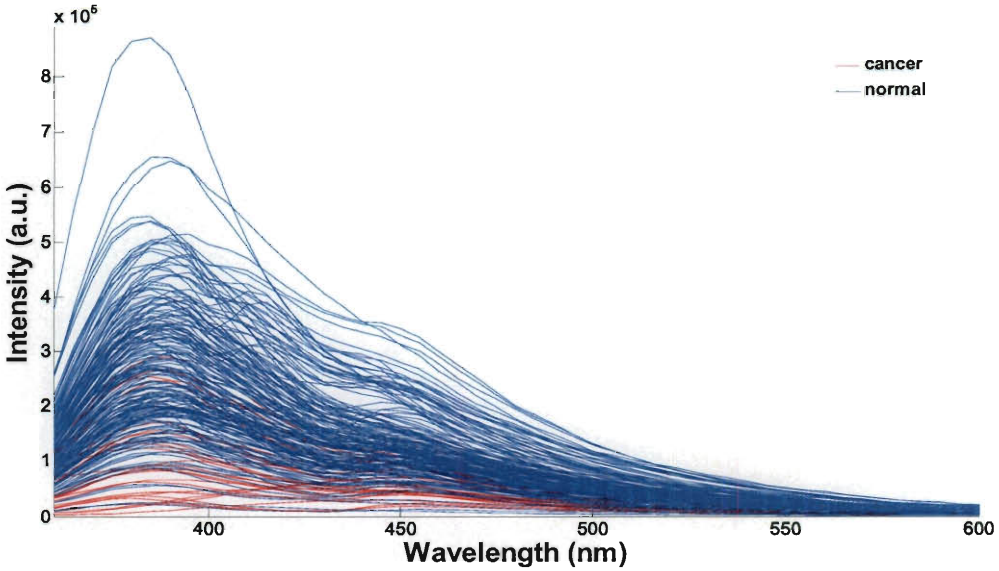

(c)

Figure 3.1- Fluorescence emission spectra of all the cancer and normal spectra used in classification. Excitation wavelength is at (a) 270nm, (b) 300nm and (c) 340nm. Cancer group has 25 and normal group has 180 measurements.

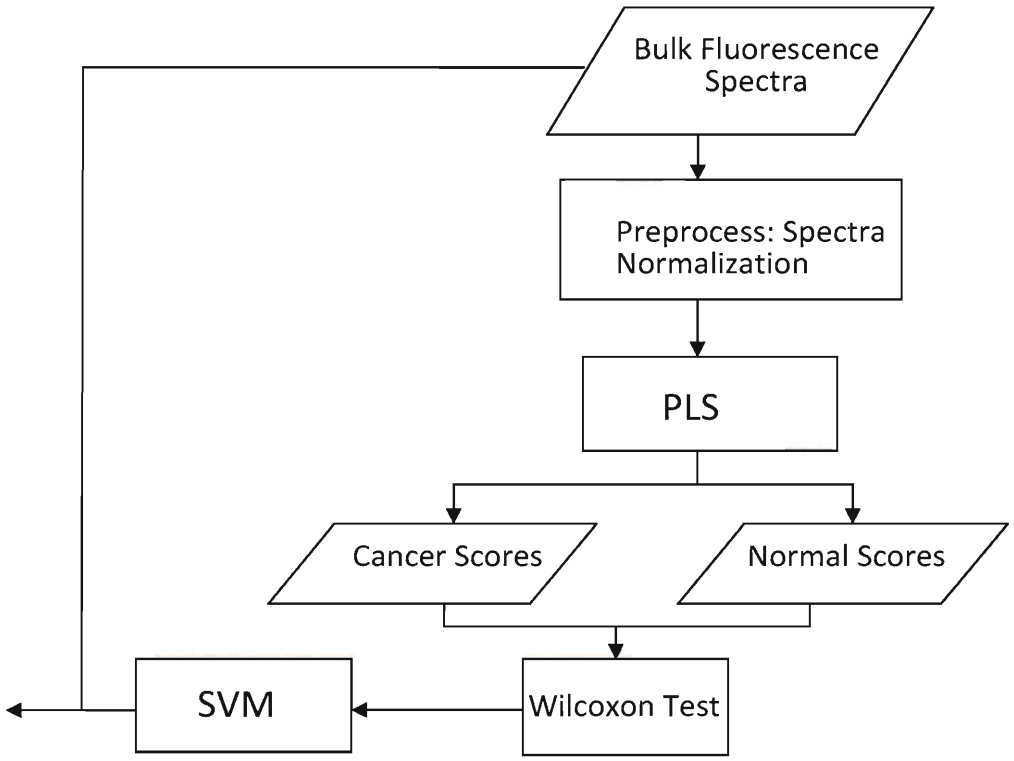

Figure 3.2- Flow chart of the classification algorithm development for the problem of discriminating between cancer and normal groups (cancer vs. normal).

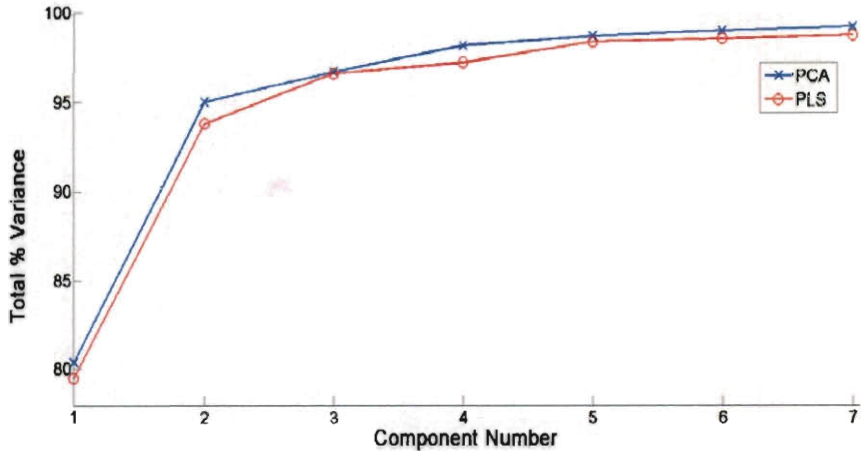

Figure 3.3- Variance plot for cancer vs. normal discrimination at 270nm excitation: Plot of the total percentage variance explained in the spectral dataset obtained at 270nm excitation for discrimination between cancer and normal groups. The total percentage variance in the original spectral data is shown as a function of PLS and PCA components.

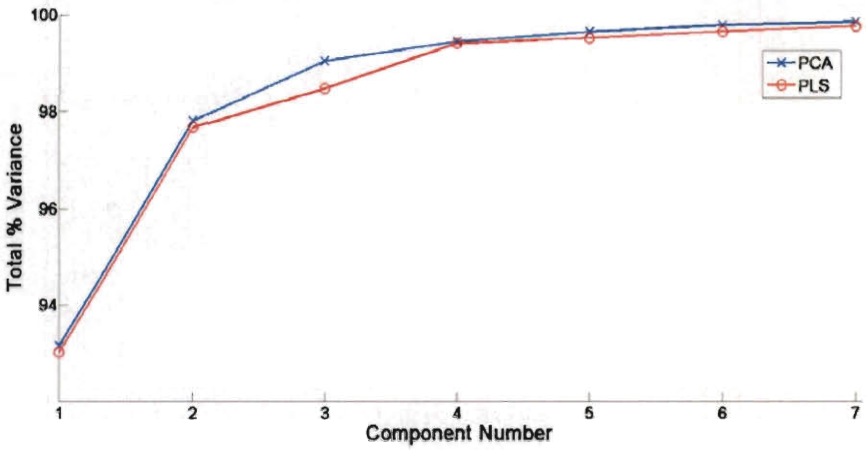

Figure 3.4- Variance plot for cancer vs. normal discrimination at 300nm excitation: Plot of the total percentage variance explained in the spectral dataset obtained at 300nm excitation for discrimination between cancer and normal groups. The total percentage variance in the original spectral data is shown as a function of PLS and PCA components.

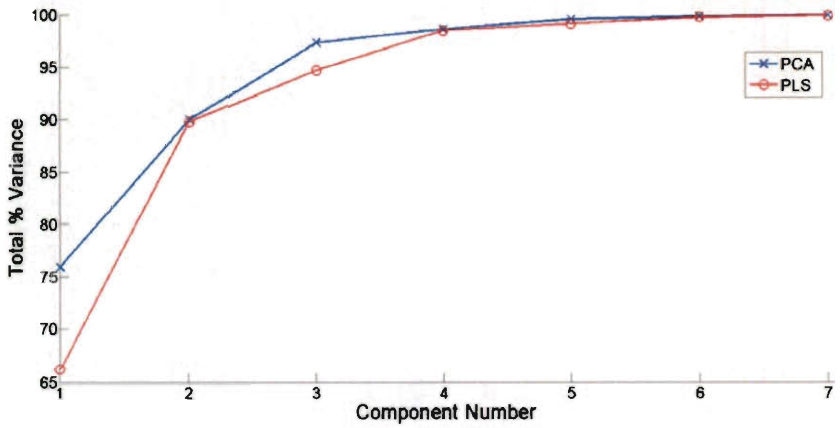

Figure 3.5- Variance plot for cancer vs. normal discrimination at 340nm excitation: Plot of the total percentage variance explained in the spectral dataset obtained at 340nm excitation for discrimination between cancer and normal groups. The total percentage variance in the original spectral data is shown as a function of PLS and PCA components.

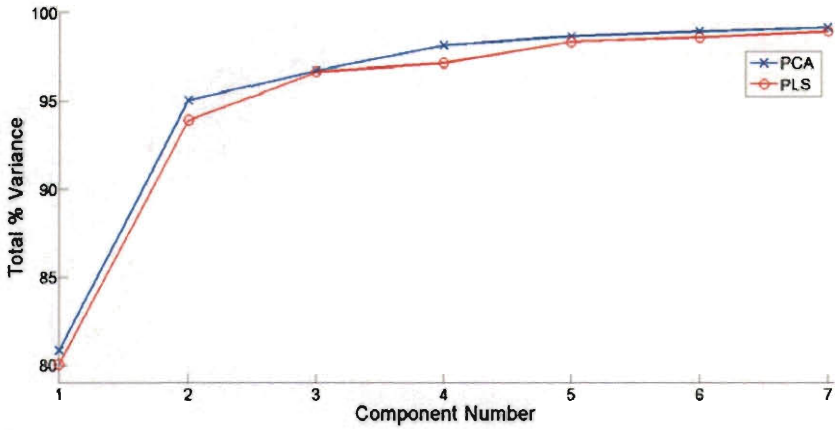

Figure 3.6- Variance plot for cancer vs. noncancer discrimination at 270nm excitation: Plot of the total percentage variance explained in the spectral dataset obtained at 270nm excitation for discrimination between cancer and noncancer groups. The total percentage variance in the original spectral data is shown as a function of PLS and PCA components.

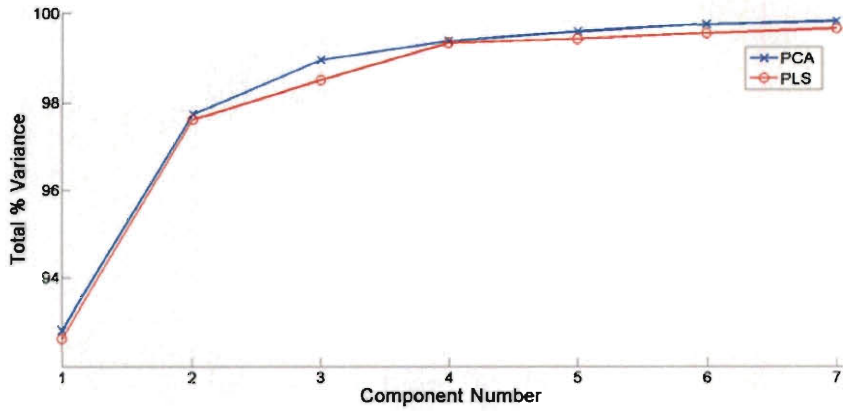

Figure 3.7- Variance plot for cancer vs. noncancer discrimination at 300nm excitation: Plot of the total percentage variance explained in the spectral dataset obtained at 300nm excitation for discrimination between cancer and noncancer groups. The total percentage variance in the original spectral data is shown as a function of PLS and PCA components.

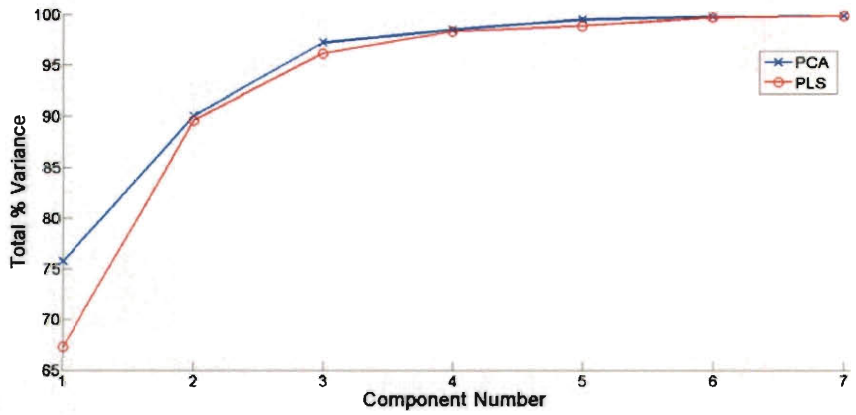

Figure 3.8- Variance plot for cancer vs. noncancer discrimination at 340nm excitation: Plot of the total percentage variance explained in the spectral dataset obtained at 340nm excitation for discrimination between cancer and noncancer groups. The total percentage variance in the original spectral data is shown as a function of PLS and PCA components.

For 270nm of excitation, the data matrix size from the spectral dataset was (205x46) i.e. consisting of 205 feature vectors (measurements) and 46 attributes (emission intensity data points). The specificity was 93.3% and the sensitivity was 96% with an AUC of 0.986 for discriminating between cancer and normal groups. Also attributes composed of the scores of the PLS components were used as input features to the SVM for classification. As noted in Section 3.4.1, PLS is a data compression method

which seek significant variations within the entire spectral data set that also have maximum covariance with the labels and then delineates the data set as a small set of component spectra or PLS components (PLS-C) and corresponding scores. PLS was applied to the fluorescence spectroscopic data. The components that contributed to 99% of the total variance in the dataset were selected and the wilcoxon rank test was used to determine which of these had scores that showed statistically significant differences between the two groups for the classification problems, cancer vs. normal and cancer vs. noncancer. The PLS-Cs that had scores which showed statistically significant differences ($p < 0.05$) were used as input features for the SVM classification. Figures 3.3-3.8 shows plots of total variance in the spectral data accounted for by the PLS and PCA components for each of the classifiers. In the variance plots, the contributions of the PLS-Cs and PCs to the total variance in the data are plotted against the factor numbers or the PC numbers. So the notation is: factor number 1,...n is PC1,... PCn for PCA components and PLS-C1,....PLS-Cn for PLS components. It can be observed that for each wavelength, in general the first few PLS-Cs had huge contributions to the amount of variance in the data while the higher order PCS contribute very little. Also, generally, the total percentage variance explained in the spectral data is higher for the PCA components compared to the PLS components. This may be due to the fact that PCA seeks variations without regard to the labels while PLS seeks variations that have covariance with the labels. Tables 3.2 and 3.3 show the PLS components that have statistically significant differences for the cancer vs. normal and cancer vs. noncancer discrimination problems respectively. As shown in Table 3.2, at the significance level of $p < 0.05$, PLS-C2 ($p=.047$) and PLS-C4 ($p=0.03$) were statistically significant. At $p<0.005$, PLS-C1 ($p=0.004$) and at $p < 0.0005$, PLS-C3

($p=3.4x10^{-5}$) exhibited statistically significant differences for discrimination at 270nm excitation. Tables 3.4 and 3.5 show the classification results for when the spectral variables were used as input to the classification algorithm. It can be observed that the classification results for 270nm excitation is competitive with the results at the other wavelengths. Classification results based on the PLS-C feature set (PLS-C1, PLS-C2, PLS-C3, PLS-C4) yielded a specificity of 90.6% and a sensitivity 88% as shown in Table 3.6. This shows that good classification could be obtained from a reduced feature size of only 4 attributes.

Wavelength	P-Value		
	P <0.05	P<0.005	P<0.0005
270	PLS-C2,PLS-C4	PLS-C1	PLS-C3
300	PLS-C2,PLS-C4	PLS-C1,PLS-C3	
340	PLS-C3	PLS-C2	

Table 3.2- This shows the PLS components (PLS-Cs) that have statistically significant differences for discrimination between the cancer and normal groups.

Wavelength	P-Value		
	P <0.05	P<0.005	P<0.0005
270	PLS-C2	PLS-C1, PLS-C4	PLS-C3
300	PLS-C2,PLS-C4	PLS-C1,PLS-C3	
340		PLS-C2	

Table 3.3- This shows the PLS components (PLS-Cs) that have statistically significant differences for discrimination between the cancer and noncancer groups.

Wavelength	Classification results			
	Sensitivity	Specificity	Accuracy	AUC
270	96	93.3	93.7	0.986
300	100	93.9	94.6	0.981
340	96	99.4	99	0.984

Table 3.4- This shows the SVM classification performance for cancer vs. normal with the spectral data as features.

Wavelength	Classification results			
	Sensitivity	Specificity	Accuracy	AUC
270	96	93.3	93.7	0.986
300	96	92.78	93.17	0.962
340	88	90	89.77	0.921

Table 3.5- This shows the SVM classification performance for cancer vs. noncancer with the spectral data as features.

Wavelength	Classification results using PLS-Cs as features							
	Cancer vs. Normal				Cancer vs. Noncancer			
	Sensitivity	Specificity	Accuracy	A U C	Sensitivity	Specificity	Accuracy	A U C
270	88	90.6	90.2	0.921	88	90.0	89.76	0.916
300	88	93.9	93.2	0.910	84	88.9	88.29	0.87
340	88	97. 8	96.6	0.930	80	81.1	81	0.833

Table 3.6- Classification results of the SVM trained on the PLS components (PLS-Cs) showing statistically significant differences for the two classification tasks: cancer vs. normal and cancer vs. noncancer.

Figure 3.9 depicts examples of 2-d plots of principal components. There is some obvious demarcation between the scores of the 2 groups in this simple plot for each wavelength, even though it is not possible to find any single line to clearly separate the 2 groups. The fact that the unsupervised PCA method shows some discrimination between the groups may give an indication of the usefulness of supervised learning methods which use the labels of the training data in constructing the classifier. This calls to attention the usefulness of SVMs which allow the data space (involving the PCs) to be transformed into a higher dimensional feature space and a hyperplane sought to better distinguish the two groups. Figure 3.10 shows the ROC curves for the cancer vs. normal discrimination using the spectral data as SVM inputs. The AUC values are all greater than 0.9.

At 300nm excitation, the data matrix size from the spectral dataset was (205x51) and when it was used as the original input space for the SVM, the specificity obtained

was 93.9% and the sensitivity was 100% with a ROC AUC of 0.981 for discriminating between cancer and normal tissues as shown in Table 3.4. Figure 3.4 shows that when PLS and PCA were applied, the first 3 components yielded about 99% of the variance and each yielded statistically significant differences between the cancer and normal groups. Figure 3.1(b) suggests, the spectra of the cancer and normal groups have similar intensity values. When the peak emission intensity values were compared, there wasn't any significant difference between the normal and cancer groups at the significance level of $p<0.05$. Classification results based on the PLS component feature set yielded a specificity and sensitivity of 93.9% and 88% respectively.

At 340nm excitation, the data matrix size from the spectral dataset is (205x57) and the results of the trained SVM for discrimination for cancer vs. normal are tabulated in Table 3.4. It should be noted that even though the accuracy of 99% is higher than that for 270nm which is 93.7%, the AUC of 0.984 is slightly less than the AUC for 270nm excitation which is 0.986. In the literature, the overwhelming majority of studies report either the AUC or the specificity/sensitivity/accuracy for the evaluation of an algorithm. When the goal is to compare the performance of algorithms, providing both metrics may be more useful than just using either one in the evaluation process.

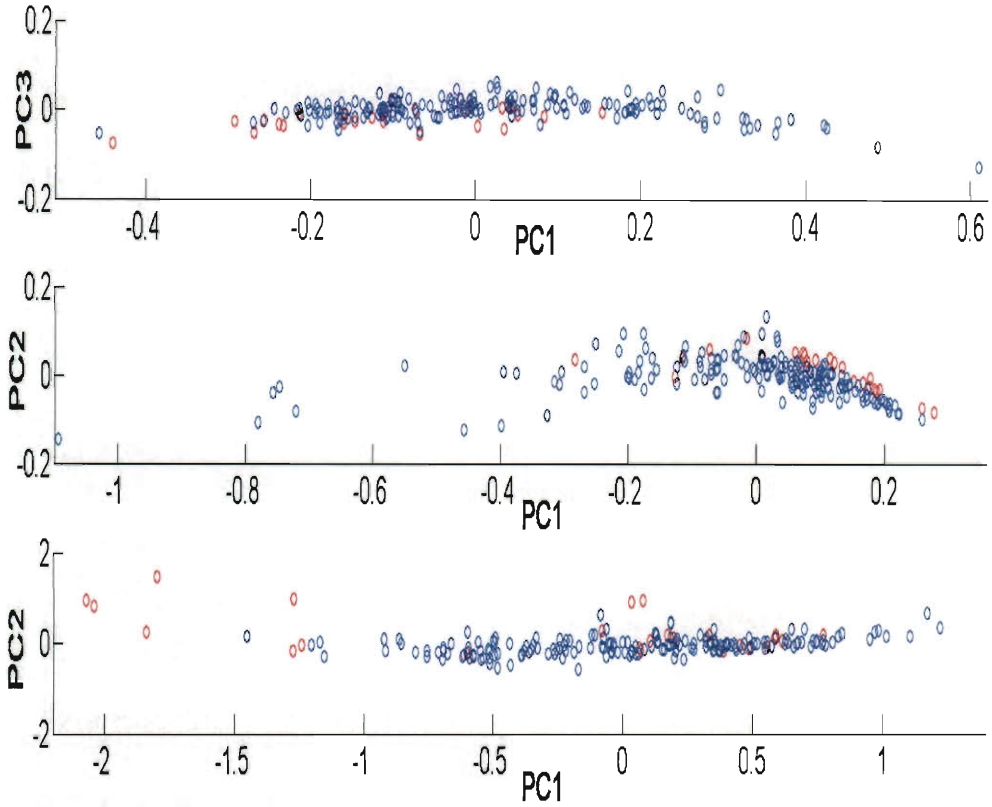

Figure 3.9- Score plots of principal components for the discrimination of cancer and normal groups. Topmost graph is that of PC1 and PC3 for 270nm excitation. Middle plot is that of PC1 and PC2 for 300nm excitation. Bottom plot is that of PC1 and PC2 for 340nm excitation.

For the cancer vs. noncancer discrimination, the data matrix for each excitation wavelength had a length of 223 corresponding to the total number of measurements. This noncancer group was composed of the data from benign neoplasm (8 measurements) and endometriosis (10 measurements) in addition to the measurements from the normal group. Endometriosis is a painful condition in which tissue similar to the endometrial layer lining the uterus is found on the ovary, and benign neoplasms are tumors that are not malignant and are unlikely to turn into cancer. The variance plots for each of the classifiers for the cancer vs. noncancer discrimination is provided (Figures 3.6-3.8). It is obvious from the plots that the first few components are responsible for the most

variation in the dataset. Similar to the cancer vs. normal case, the PLS components explain less of the variance in the spectral dataset compared to the PCA components. Table 3.3 summarizes the PLS-Cs that showed statistically significant differences between the two groups. All the PLS-Cs that exhibited statistically significant differences for the comparison between the cancer and noncancer groups were also statistically significant for the comparison between the cancer and normal groups. For the classification at 340nm excitation, only one PLS-C showed statistically significant difference for significance levels of $p < 0.05$. But, the SVM algorithm requires at least two features for classification; a significance level of 15% ($p < .15$) was able to select the needed feature size and hence was used. PLS-C1 and PLS-C2 were selected to be used for the cancer vs. noncancer discrimination. Table 3.6 summarizes the classification results using the PLS-Cs selected by the wilcoxon test, and it showed generally good values for AUC and specificity/sensitivity/accuracy. The cancer vs. noncancer classification followed the same process as outlined in the flowchart of Figure 3.2, the only difference being that the "Normal Scores" is replaced by "Noncancer Scores".

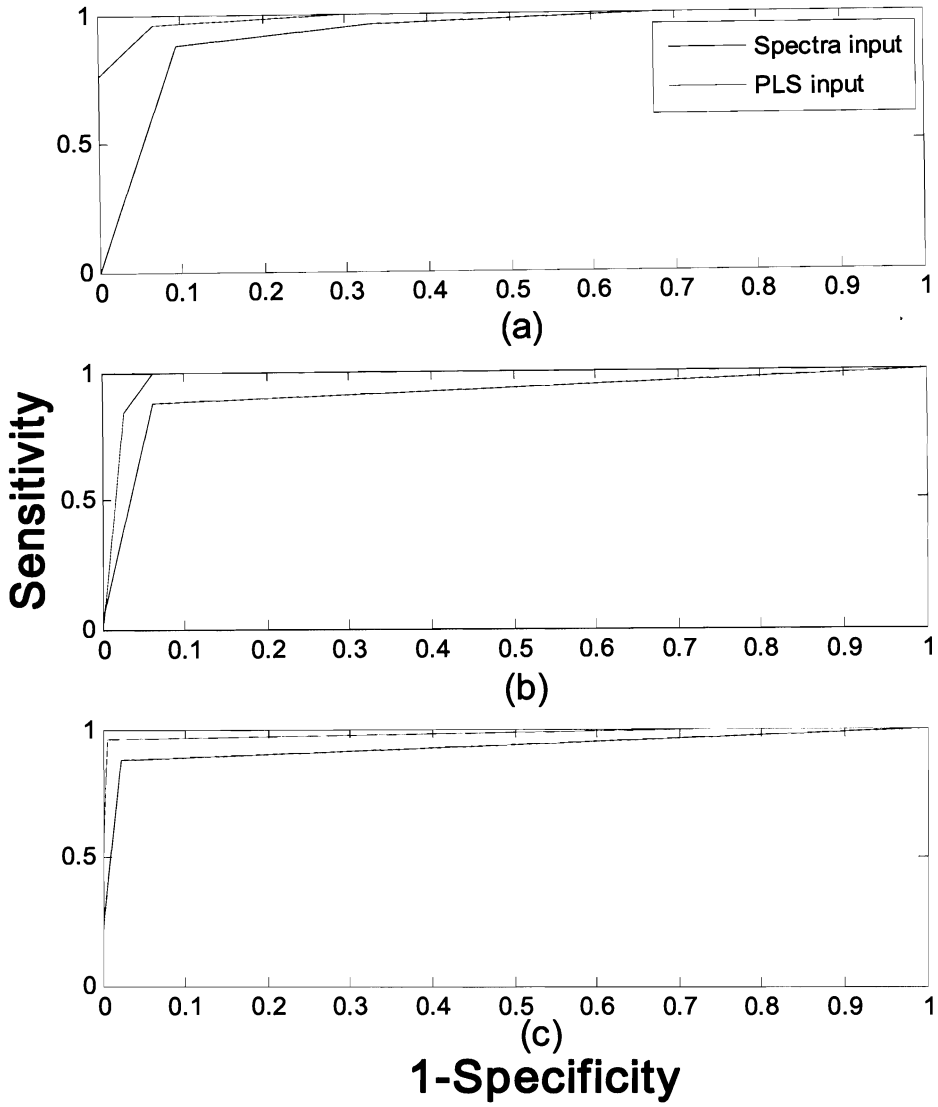

Figure 3.10- This shows the ROC curve for discrimination between cancer and normal groups when the SVM was trained on the spectral data, and when the SVM was trained on diagnostically relevant PLS-Cs. Results are shown for: (a)270nm, (b)300nm and (c)340nm of excitation.

3.6 Discussion

Limited work has been done on ovarian fluorescence spectroscopy, as compared to other organ sites. Brewer *et al.* has explored fluorescence spectroscopy and microscopy of the ovary.[54,55] Kamath *et al.* reported the multivariate analysis of ovarian tissue fluorescence spectra in which they studied tissues in three main histopathological groups: cancer, normal and benign. Features including the mean, median, spectra residual and standard deviation of the emission spectra were used as inputs into a kNN algorithm for classification.[49] They were able to obtain a specificity of 100% and a sensitivity of 90.9% for classification. Whilst this study has great results, they used a small data set involving only 20 patients and a total of 97 measurements with only one wavelength of 325nm. The data set employed in our study is more than twice the size of that used in the aforementioned study and we analyzed data at multiple excitation wavelengths.

The average emission peak for the tissues at 270nm of excitation occurs at around 325nm emission, indicating the presence of tryptophan residues with some contribution from the other aromatic acids phenylalanine and tyrosine. The most dominant fluorophore excited at this wavelength is tryptophan, and there is regular energy transfer from tyrosine to tryptophan. There is an observed increase in the fluorescence emission peak in the cancer group relative to the normal group as shown in Figure 3.1(a). This may be attributed to an increase in the concentration of the aforementioned fluorophores. Even other spectroscopy modalities besides fluorescence, suggest that these aromatic amino acids have varying contributions to a spectrum depending on tissue histopathology. For example a Raman spectroscopy study by Draga *et al.* reported statistically significant differences (at least $p< 0.01$) between cancer and normal tissues at infrared wavelengths

that were attributed to phenylalanine (1003cm^{-1} and 1208cm^{-1}), tyrosine (1170cm^{-1}) and tryptophan (1208 cm^{-1}).[72] Other studies involving other tissue organs have also observed this change.[73] The great classification results we obtained from the spectroscopic studies suggest the usefulness of 270nm excitation for fluorescence imaging applications since the technique relies on spectrally selective excitation and emission wavelengths. A diagnostically relevant excitation wavelength is crucial in this application which enables the imaging of large areas of tissue. One can easily use a band pass filter selecting wavelengths around the peak emission maxima of the spectrum to collect the fluorescence images of tissues. And the of the high sensitivity and specificity SVM algorithm, automated diagnosis of cancer and even precancer tissues that have known precancerous lesions can be realized.

At 300nm of excitation, the average emission peak of the spectra shown in Figure 3.1(b) occurs at around 315nm. It is likely that tyrosine fluorescence contributes to the peak just as it did for 270nm excitation. The emission peak intensity didn't show statistically significant differences between the two groups as it did for 270nm excitation. It has been reported that unlike for the UVC wavelength, tyrosine and phenylalanine may not be excited at 300nm.[73,74] Hence it is possible that the lack of contribution from tyrosine and phenylalanine to the spectra is partly responsible for the small peak intensity difference between the two groups. Nonetheless we noted higher average peak intensity in cancerous compared to normal tissues and this observation is made in other studies as well. In a seminal study by Yang *et al.*, the spectra of excised cancerous tissues showed higher fluorescence intensity at an emission peak of 340nm than normal tissue for 300nm excitation.[41]

The emission spectrum for 340nm of excitation has average peak emission at 390nm and a less prominent peak at 460nm as observed in Figure 3.1(c). Also there is a prominent dip at around 430nm of emission which is attributed to oxyhemoglobin absorption in the tissue. The measured spectra was different for the cancer and normal groups. As measured by the wilcoxon ranksum test, there was a statistically significant difference between cancer and normal groups at the emission peak of 390nm ($p < 4.5 \times 10^{-4}$). It was observed that as the wavelength of excitation increases, the average peak emission fluorescence of normal tissues get larger than that of cancer tissues. This may suggest that some of the prominent fluorophores that get excited at longer wavelengths have smaller concentrations in cancer tissues. Studies conducted using excitation around the 340nm wavelength, include one by Ramanujam *et al.* in which a 337 nitrogen laser was used to acquire the spectra of preneoplastic, neoplastic and normal tissues of the cervix.[75] They noted a decrease in the fluorescence signal of tissues with the progression of cancer. This was attributed to a decrease in collagen fluorescence and an increase in oxyhemoglobin attenuation, among other factors. Another study at the same wavelength of excitation was used to analyze spectra from colon sites of patients. Also in this study, spectroscopic differences were observed between the spectra of neoplastic and non-neoplastic tissues and a diagnostic algorithm exploiting the differences, obtained a sensitivity and specificity of 80% and 92% respectively for distinguishing between the two tissue types.[76] Georgakoudi *et al.* combined the techniques of fluorescence and diffuse reflectance spectroscopy to extract the intrinsic NAD(P)H and collagen fluorescence from bulk Barrett's esophagus tissue fluorescence *in vivo*.[77] They found that the intrinsic NAD(P)H fluorescence was substantially smaller and intrinsic collagen

fluorescence greater in non-dysplastic tissues compared to dysplastic tissues thus shedding light on the biological basis of the spectral differences that occur at around 340nm excitation. Findings from other studies also suggest an increase in NADH fluorescence with dysplasia.[36-39] The reason that can be attributed to the increase in the NADH metabolic coenzyme in cancerous tissues is the higher metabolic activity in these tissues. The presence of the protein, collagen also contributes to the fluorescence at this wavelength. A breakdown of the extracellular matrix of ovarian tissue as cancer develops is responsible for the marked decrease in collagen fluorescence which has an emission maximum close to the average emission peak of 390nm observed in this report. With a sensitivity of 96% and a specificity of 99.4% for the discrimination of cancerous tissue spectra from normal spectra excited at 340nm, this wavelength is very useful for classification of ovarian tissues. Tissue excitation around this wavelength range is very common in the literature as many studies involving multiple excitation wavelengths have found that it usually is among the most significant tissue classification wavelengths.[38]

Concerns for patient safety and possible tissue mutagenicity after exposure to UV radiation are among the reasons that UVC wavelengths are underutilized for tissue spectroscopy or imaging. But it has been shown that successful studies can be conducted for excitation at low power levels that are safe.[54,78-80] Safety standards for skin exposure as established by the American Conference of Governmental Industrial Hygienists (ACGIH) puts a maximum threshold limit of radiation from broadband sources in the range 250-400nm at .003J/cm^2.[81] Spectroscopy systems for the detection of cervical cancer submitted to the FDA for approval are expected to have radiation thresholds below the limit set by the ACGIH.[81] Tissue fluorescence spectra with high signal to noise

ratio can be obtained at levels up to an order of magnitude below this threshold.[82] As safety issues can be held in check, the excellent diagnostic potential of the UVC region makes wavelengths in that range warrant further studies. The FDA has approved a number of optical systems for use in tissue diagnosis.[83,84] One such system, the WaVSTAT developed by SpectraScience and approved as an adjunctive tool to aid in colon cancer diagnosis uses laser excitation in the UV to collect fluorescence spectra to provide immediate classification of tissue into normal, precancer or cancer groups. It has been noted that while endoscopy in expert hands may achieve a sensitivity of 80% for disease detection, WaVSTAT can achieve a sensitivity of 96%.[85] But then the system has a fairly low specificity of about 75% which results in significant number of false positives.[85] The SVM algorithm outlined here may be used in such a system to achieve an acceptable specificity whilst maintaining a high sensitivity because of the NP criterion used in training. This would improve the functionality of the system as a complementary tool for diagnosis. At 270nm excitation, for cancer vs. normal discrimination, we obtained a sensitivity of 96% and specificity of 93.3% with an AUC of 0.986, excellent results for single wavelength excitation compared to that of other studies reported in the literature. The NP criterion formally stated in Section 3.3 essentially allows the training of an algorithm so as to find a decision rule that maximizes the specificity while holding the sensitivity to a high value. This threshold or significance level can be changed by the user to produce algorithms tailored to specific aims. For the classification involving the spectral dataset, we sought to guarantee a sensitivity of 88% and hence α=0.88 was used. When the dimension reduction method, PLS, was used to reduce the spectral dimension before SVM classification, we could still obtain good classification results using far

fewer attributes as shown in Table 3.6. PLS reduces the size of the attributes or feature size and not the group size so when training seeks to maximize overall accuracy, the classifier can still be prone to seeking a rule that favors the group with the larger size at the expense of the group with the smaller size. Hence the advantages of training subject to the NP criterion still hold true. For the classification involving the PLS-Cs, the desired value was α=0.8. The main aim of using the PLS selected features was to obtain acceptable classification results from a small feature size.

Traditionally, classification algorithms seek a classifier that maximizes the overall accuracy, this SVM algorithm may seek one that selectively maximizes either the sensitivity or specificity. This restriction is effective in addressing an unbalanced training data set in which one group size far exceeds that of the other group. Most diagnostic algorithms based on fluorescence spectroscopy found in the literature haven't accounted for data imbalance in binary classification. No study involving ovarian tissue fluorescence spectroscopy whether *in vivo* or *ex vivo* has addressed this. Thus the study here is the first such study to train a classifier for the diagnosis of ovarian tissues with the aim of achieving a balance in sensitivity and specificity values regardless of the data imbalance between disease and control groups. Moreover, to the best of our knowledge, this study is the first to train an SVM on any optical spectroscopy data to tackle the skewed classification results that can occur when training data is not balanced. Another important aspect that differentiates the SVM algorithm employed here is that the user specified parameters are bounded and so the beginning and end points don't have to be chosen subjectively. This renders the algorithm far less arbitrary. In a study by Zhu *et al.* in which SVM was used to differentiate between 27 malignant and 94 nonmalignant

breast tissue samples, they obtained a sensitivity of 28.1% and a specificity of 98.1%, and concluded that the skewed classification result is likely due to the data imbalance.[45] The nonmalignant group was just over 3 times larger than the malignant group in their study and they obtained skewed results, in our study the normal group is more than 7 times larger than the cancer group and the imbalance is even greater for the classification between the cancer and noncancer groups. Yet our classification results are fairly unbiased. In general, for binary classification, one is going to find that the diseased group is going to be larger than the control group and when a classification rule seeks to maximize overall accuracy or minimize the rate of misclassification, the classifier may produce skewed results. The NP criterion, as applied here, gives us control over this by modulating the threshold.

The major disadvantage of empirical methods that directly use features from the acquired spectrum for diagnosis is that it provides limited knowledge of the changes in the tissue biochemistry and morphology that is ultimately reflected in the changes in the acquired spectra. Physically based methods to extract parameters directly related to the structure of tissues and cellular metabolic processes from a model of tissue fluorescence based on the radiative transport theory or monte carlo methods can be used to elucidate the disease process. Nonetheless, the shear diagnostic ability of empirical methods is obvious and this has lead to physicians in hospitals adopting systems based on empirical analysis of fluorescence spectroscopy for use as complementary diagnostic tools.

3.7 Conclusion

Fluorescence spectroscopy provides a real time technique to analyze morphological and biochemical processes that accompany tissue changes leading to cancer. This makes it viable as a diagnostic tool for detecting cancer and pre-cancer in many organ sites. The use of selected multiple excitation wavelengths throughout the UV and visible regions have shown that the discrimination of cancer and precancer from normal tissues can be done with sensitivities and specificities that are higher than the one provided by current methodologies. However, the use of unbalanced data in which one group size is considerably larger than the other in training classifiers may make these algorithms prone to skewed results in favor of the group with the larger size. Training classifiers subject to the NP criterion in which we maximize the specificity while setting constraints such that we are assured a high sensitivity value is a way that prevents the classifier bias. In standard cases, the larger group is the normal or control group, which means that classifiers may obtain results that have a high specificity but low sensitivity. In NP classification, when we seek a classifier that sets constraints to achieve high sensitivity values rather than one that seeks overall maximum accuracy, we can obtain high sensitivity results and still get high specificity values. We trained an SVM algorithm subject to the NP criterion and we obtained excellent sensitivity and specificity values for the discrimination of ovarian cancer fluorescence spectra from normal fluorescence spectra for each of three excitation wavelengths 270nm, 300nm and 340nm. Excellent sensitivity for identification of cancerous tissues results in a tool that can be used for ovarian cancer detection. Moreover, the algorithm may be employed in demarcating tumor margins and for the monitoring of treatment including response to photodynamic

therapy, when used for *in vivo* applications. We can also select the user specified significance level to guarantee a high specificity value, while maximizing the sensitivity. This type of classifier can especially be useful in the selection of optimal biopsy specimen and reducing the problematic cases of taking unnecessary biopsy samples. This in turn cuts down the time needed for traditional diagnosis and also the amount of sedatives that is used during conventional biopsy. Moreover, 270nm gave us great classification performance that was comparable to that of the diagnostically important wavelength of 340nm. This underscores the importance of this wavelength and the underutilized UVC region in developing classifiers with high diagnostic accuracy for the detection of cancer. Further studies including even larger sample sizes than the one in this study need to be done to access the potential of this wavelength region. *In vivo* studies utilizing low power levels of excitation, to safeguard against tissue mutagenecity, are also warranted. Other organ sites, especially ones that are known to develop cancer in its superficial layers such as the cervix, may also benefit from diagnostic algorithms in this fluorescence wavelength region. The potential for detecting precancerous lesions and other tissue abnormalities such as inflammation in these organ sites should also be studied. Fluorescence spectroscopy systems offer a tool for the objective and automated diagnosis and screening of cancer and the use of well tailored diagnostic algorithms such as the NP SVM algorithm used in this study would further improve the capabilities of these systems.

[1]Chapter 4:

Needle Compatible Reflectance Fiber Bundle Endoscope

4.1 Introduction

We developed a miniature-sized high-resolution low-cost reflectance-mode fiber microscope (RFM) aimed at optical tissue biopsy applications that uses polarized imaging configurations to suppress background noise from specular reflectance. The RFM is equipped with an air-cooled light-emitting diode illumination module and a single 450-μm outer-diameter fiber bundle image guide which is compatible with a 20-gauge needle. The dual illumination and image acquisition nature of the fiber bundle simplifies the system and reduces the total cost. Imaging tests with a US Air Force resolution target demonstrate a lateral resolution of ~3.5 μm. The performance of the imaging system was evaluated by examining samples of green onion skin cells, cultured breast cancer cells, and excised human oral cancer tissue. Still and video rate images are obtainable in reflectance mode using intrinsic contrast.

Standard histopathology requires surgical removal of suspect tissue for examination, limiting its applicability in routine cancer screening and low-invasive cancer diagnosis. Less invasive techniques, from core needle biopsy to fine-needle aspiration biopsy, must remove a tiny piece of the suspect lesion from its surrounding tissue. To better examine the suspect lesion, endoscopic imaging techniques have advanced to employ a wide range of modalities including fiber scanning confocal

[1] This has been adapted from reference 20

microscopy in both reflectance[86-88] and fluorescence[89,90] modes. These techniques employ an optical fiber or fiber bundle to view the surface of interior-body cavities. The optical fibers are illuminated at the proximal fiber end and images are created by scanning mechanisms positioned at either the distal or proximal ends of the fiber. These types of systems can capture point by point a high-resolution image from a larger field of view.[91-93] Furthermore, because high energy can be channeled to each image pixel, the sensitivity of the system can be very high.

Recent advances in simple, low-cost optical-fiber based fluorescent imaging systems have permitted the fabrication of this type of endoscopic imaging apparatus with limited resources.[18,19,94] This imaging technique is based on transferring inner-body images outside the body via a coherent multi-mode fiber bundle, and then directly capturing the image using an off-the-shelf digital camera. The resolution of modern digital cameras is such that the image resolution is limited by the individual fibers of the fiber bundle. In addition, imaging using a digital camera offers the advantage of high imaging speed and the possibility of capturing single image frames without scanning. A fluorescent-mode fiber endoscope has been developed by Muldoon *et al.* that achieves a resolution of ~4.4 μm.[18,94] We are developing a high-resolution (~3.5 μm) reflectance-mode endoscope that is flexible, compatible with a 20-gauge needle, and that can generate still and video rate images from intrinsic contrast of biological structures. Reflectance-mode endoscopic imaging can potentially complement fluorescence imaging by capturing information not available in fluorescence mode and by functioning in situations when fluorescent imaging is hard to achieve. In this study, we present a needle-

based high-resolution reflectance-fiber microscope (RFM) developed for optical tissue biopsy applications.

4.2 System Assembly

The RFM was assembled on a portable 18 × 24 × 1/2 inch^3 aluminum breadboard to facilitate eventual clinical trials. As shown in Figure 4.1, an air-cooled light-emitting diode (Luxeon; white LED, model LXHL-NWE8; blue LED, model LXHL-NRR8) served as the illumination source to keep the RFM as compact as possible and also reduced the system cost.

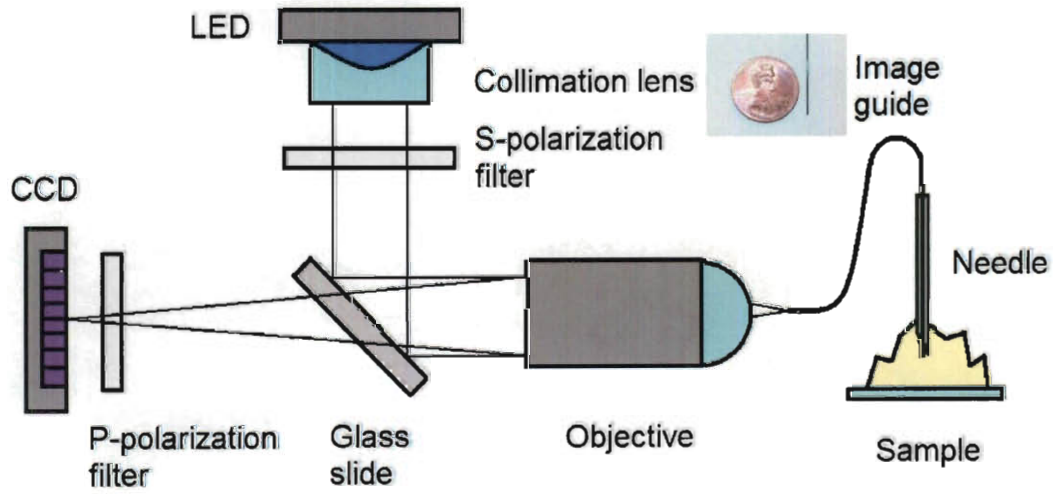

Figure 4.1- Schematic of the reflectance fiber imaging system

The light from the LED is collimated by an integrated collimating lens and passes through a linear polarizer (Figure 4.1), after which the polarized light is reflected by a glass slide positioned at ~45° (with respect to the beam trajectory) and projected onto an

infinity-corrected 10× objective lens (Newport, model: L-10x, 0.25NA). The objective lens and a fiber chuck (Newport, model: FPH-DJ) are positioned with a multimode fiber-coupler positioner (Newport, model: F-915T). By careful alignment, the illumination light is focused into the incident end of a 450-μm outer-diameter fiber image guide which is positioned by the fiber chuck (Sumitomo Electric, model: IGN-037/10, 10^4 fiber elements in a picture area of 333 μm diameter, 0.35NA).[95] Finally, the imaging end of the fiber image guide is inserted into the core of a 20-gauge needle and positioned in contact with the samples. Light scattered from the samples is collected by the same illumination fiber and passes back through the same 10× objective lens and glass slide just described previously (see Figure 4.1).

A CCD color camera (Edmund Optics, model: EO-0813C) coupled with a circular polarizer filter (Nikon, 62mm) is used to sample the fiber bundle elements for image acquisition. Because the polarization orientation of the S-polarized illumination light is perpendicular to the plane of incidence with respect to the glass slide (i.e., the plane of the Figure 4.1), a significant portion is reflected toward the incident end of the fiber bundle to be delivered to the imaging end of the fiber bundle. Specular reflectance from the incident end of fiber bundle is also partly reflected away by the glass slide, and the remaining specular reflectance is further suppressed by the circular polarizer in front of the CCD camera that passes P-polarized light with respect to the plane of incidence. Theoretically, only rays that result from multiple scattering events and change their polarization to the parallel direction can be detected by the CCD camera (e.g., light scattered from the sample). Thus, noise from specular reflection from the incident end of the fiber bundle is greatly suppressed, and clearer images are collected.

4.3 Imaging Demonstration

Figure 4.2(a) shows the reflectance image of the fiber-bundle imaging end when the needle microscope is positioned in air. Light from the white LED that is reflected from the glass-air interface at the imaging end of the fiber bundle is successfully detected by the CCD camera, and individual fibers of the fiber bundle are resolved (Figure 4.2(a)).

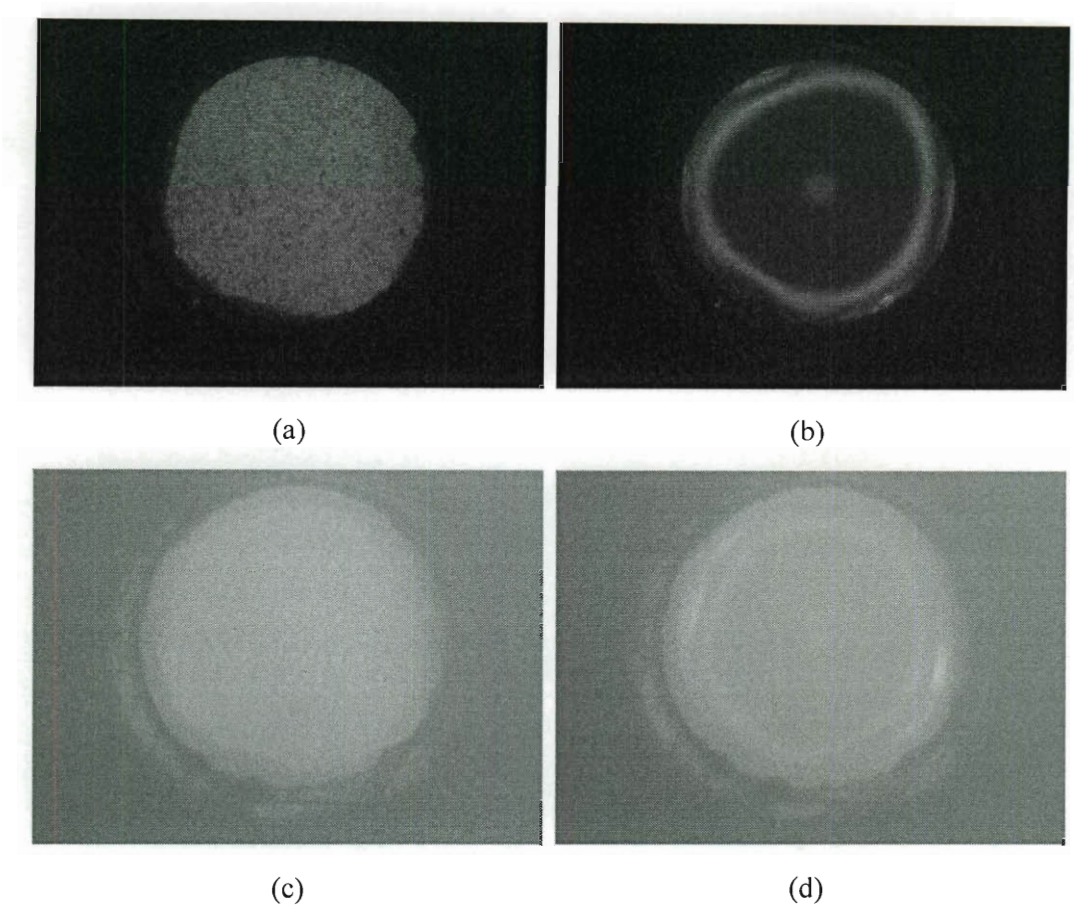

(a) (b)

(c) (d)

Figure 4.2- Reflectance images of the fiber-bundle tip glass/air interface showing greatly reduced background noise from specular reflectance with this RFM system in comparison with the non-polarized imaging system. The images (a) and (b) were obtained with cross-polarized illumination and imaging filters. For image (a), the fiber tip was in air. For image (b) fiber tip was covered with a drop of water. Images (c) and (d) were obtained without polarized illumination and imaging filters. Image (c) is with the fiber tip in air, whereas image (d) is with the fiber tip covered with a drop of water.

With the imaging needle of the RFM immersed into a vial of water or phosphate-buffered saline (PBS) solution, the RFM field of view is almost completely dark because of the close match between the refractive indices of water and the glass fiber results in dramatically reduced internal reflection from the imaging end of the fiber bundle.

Figure 4.2(b) is obtained with a drop of water covering the tip of the imaging fiber bundle, which mimics the immersion of fiber tip in water, to provide clear image features. It is clear that much less internal reflection occurs from the imaging area covered by water [Figure 4.2(b)] compared with the same area when it is exposed to air. Figures 4.2(a) and (b) were captured with the same imaging configurations and the index-matching effect is clear. When used in biological or clinical environments, the fiber-bundle tip is always covered by liquids such as body fluids, etc. Therefore, dipping the fiber-bundle tip into water closely mimics the conditions of a real imaging application. Moreover, in liquid solution, the reduced internal reflectance leads to a dark field of view and a decrease in background noise for biological imaging. Thus, light scattered by biological scatterers can be clearly distinguished and cellular images can be obtained. In comparison with the polarized reflectance-mode images in Figures 4.2(a) and (b), images shown in Figures 4.2(c) and (d) were captured with a reduced exposure time under the same imaging conditions but without the illumination and collection polarizers. The specular-reflectance noise from the optical components makes it impossible to obtain useful information from Figures 4.2(c) and (d).

The imaging ability of the RFM was tested with a US Air Force resolution target and green onion skin cells. The white LED was used to acquire the images and plots shown in Figures 4.3(a) to (c). Figure 4.3(a) shows an imaging resolution of ~3.5 μm

(~143 line pairs/mm) obtained upon imaging the US Air Force resolution target. Figure 4.3(b) shows that the contrast's decreasing slightly from low (64lp/mm) to high (128lp/mm) resolution, but it also reveals high frequency components due to the probe fibers (3.3 μm dia.). Figure 4.3(c) was obtained by using the same white LED-illuminated RFM to image the skin tissue of a green onion. The cell walls of the rectangular cells of the green onion skin[96] are clearly resolved in the image. Note that water was used in all the tests to provide refractive index matching.

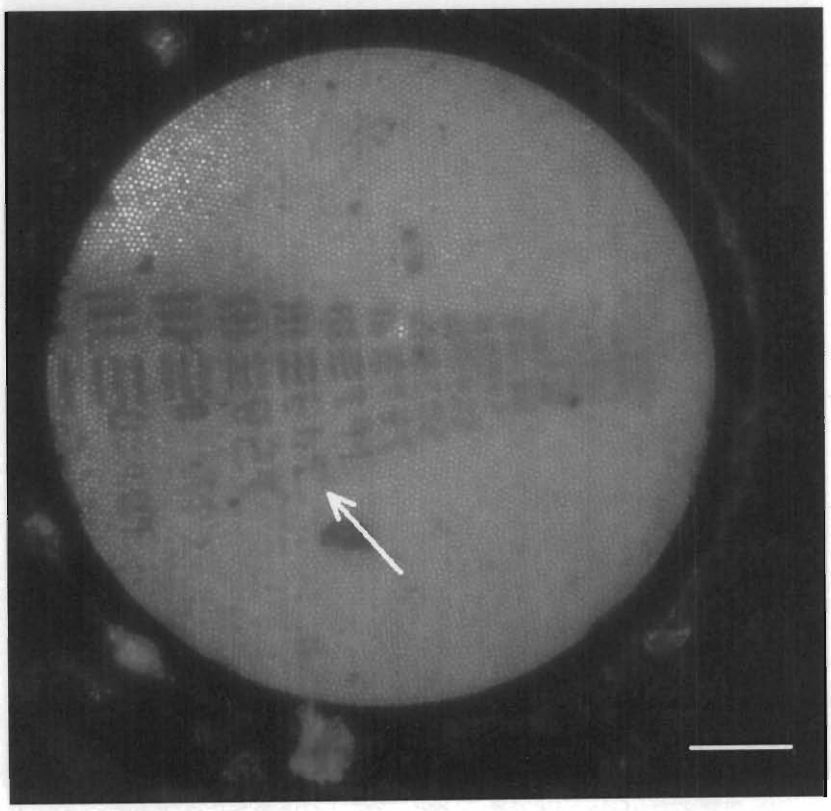

(a)

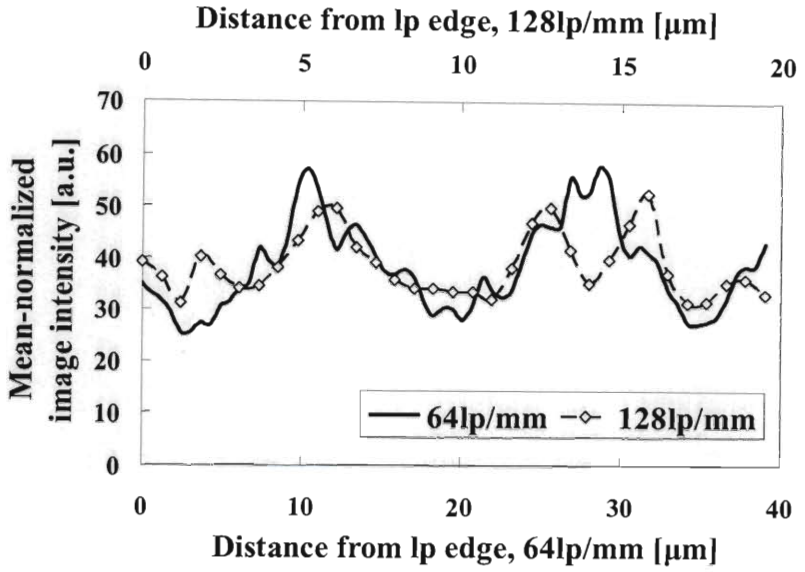

(b)

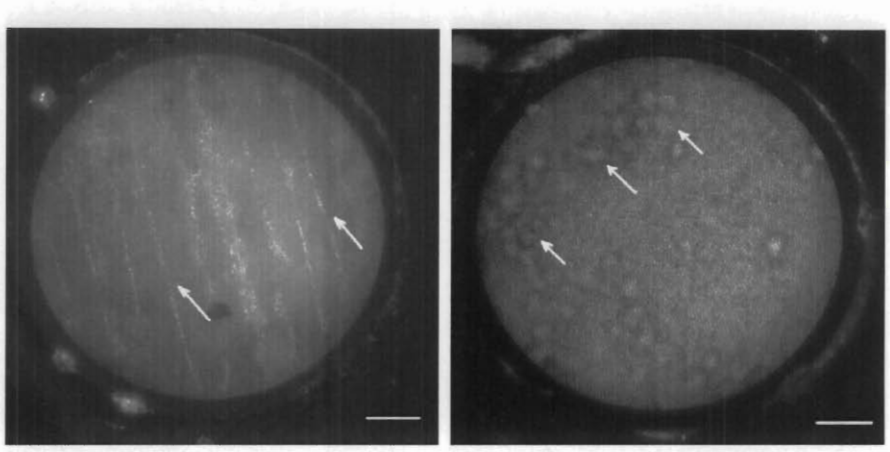

(c) (d)

Figure 4.3- Processed endoscopic images of (a) USAF resolution target showing the resolution of ~143lp/mm, acquired with white LED illumination, (b) cross sections of two resolution line-pair sets showing both the line-pair intensity variation and variation due to probe fibers (3.3μm dia.), (c) onion skin cells, where arrows show the resolved cell walls, acquired with white LED illumination, and (d) cultured SKBR3 cancer cells, where the arrows indicate resolved single cells, acquired with blue LED illumination. (Scale bar: 50μm)

The LED light source is cost effective and is easy to change. An air-cooled blue LED was used to image cultured SKBR3 human carcinoma cells. Before imaging, SKBR3 carcinoma cells were cultured in a 6-mm plate at 37 °C for 2 days. We immersed the fiber-bundle tip into the culture medium through a needle and focused onto a group of cancer cells attached to the culture plate. As shown in Figure 4.3(d), the cancer cells can be visualized with the RFM (using blue-LED illumination). The same RFM was also tested using excised human oral cancer tissue obtained from the Cooperative Human Tissue Network (CHTN).

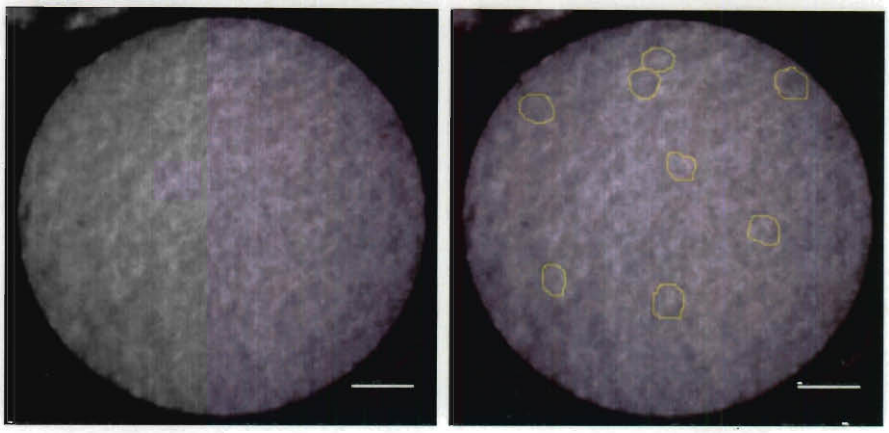

(a) (b)

Figure 4.4- Endoscopic images of excised oral cancer tissue (a) processed image showing cellular structures, and (b) processed image with drawing lines indicating the estimated cell boundaries. (Scale bar: 50 μm)

The tissue was put in a culture plate with PBS, which was then placed on a two-dimensional translation stage. The needle and fiber-bundle tip were inserted into the tissue sample and cellular structures were visualized, as shown in Figure 4.4. The same RFM used to image the reflectance from a dust particle in liquid solution resulted in single-pixel fiber resolution.

In this study, we report a high-resolution RFM developed for optical-tissue biopsy applications. The resolution of this fiber microscope is limited by the fiber size of the imaging fiber bundle. For the specific fiber-bundle image guide presented in this study, the resolution is ~3.5 μm. The reported RFM system uses the same fiber-bundle guide for both illumination and imaging. A pair of cross-polarized filters is used in addition to the fiber-bundle guide to achieve high-resolution reflectance-mode microscopic imaging. The fiber-bundle guide is 450μm in diameter, which makes it compatible with current clinical needle tissue biopsy systems. This RFM system can work without external agents when there is enough endogenous imaging contrast, and it can also be used with functionalized contrast agents to enhance image quality and to acquire targeted images for diagnosis. Moreover, with easy filter changes, the current RFM system can be easily converted to a fluorescence-mode needle-biopsy imaging system similar to the one developed by Muldoon *et al.*.[94]

4.4 Conclusion

A low-cost endoscopic RFM system has been developed using polarized imaging strategies to achieve real-time images of biological samples. A proof-of-concept study, demonstrating cellular level images obtained with the compact fiber microscope has been presented. Images including that of human tissue and plants have been used to demonstrate the system's capability. Future work including the use of LEDs of varying illumination wavelengths and power are being investigated to further evaluate and enhance the imaging potential of the needle-compatible RFM endoscope.

[1]Chapter 5: FTIR Absorption Spectroscopy for the Detection of Cervical Cancer: Spectroscopy of Formalin Fixed Tissues

5. 1 Introduction

FTIR spectroscopy depends on the absorption and vibration of molecules in the infrared region (400-4000cm^{-1}) of the electromagnetic spectrum. Analysis of FTIR spectra represents a powerful tool that can access the physiological and biological modifications of tissues that are related to changes in molecular structure and molecular interactions. The IR spectra of various organ sites show many similarities in their main spectral features since biological tissues share the same basic constituents which are proteins, carbohydrates, lipids and nucleic acids.[98] IR spectroscopy presents a promising potential to detect tissue abnormalities which arise with the onset of disease.[99] A number of groups have reported on the ability of FTIR spectroscopy and microscopy to convey useful information that may be employed by pathologists in the classification of tissue samples. It has been shown that Infrared (IR) spectroscopy may be used to distinguish normal and cancerous colorectal cells, normal and neoplastic lung tissues, normal and leukemic lymphocytes; normal, dysplastic and malignant ovarian tissues and normal and carcinoma breast tissues.[100-104] Previous studies have reported on the analysis of the FTIR spectra of various types of cervical tissues including dysplastic squamous epithelium,[105] cervical adenocarcinoma,[98] malignant radiotherapy[106] and normal tissues.[107]

Cervical cancer is a prevalent gynecological cancer among women both in the developed and the developing world. In the United States, the incidence and mortality of the disease has declined considerably over the past several decades due to frequent use of

[1] This work is adapted from Reference 97

the Pap smear to detect pre-invasive cases of cervical cancer. Yet, a considerable number of cases are still diagnosed during the late stages of the disease when the tissues are clearly malignant. Moreover, in the developing world, which account for about 80% of new cases of cervical cancer, many women have never had a Pap smear.[108] These reasons underscore the need for research into finding new diagnostic protocols for cervical cancer.

Our aim in this study is to provide an exhaustive analysis of the differences between the spectra of normal and cancerous cervical tissues and to develop algorithms that may be useful in the diagnosis of cervical cancer. Our methods of analysis include ratio analysis of pertinent bands in the fingerprint region, t-test measure of significant differences and multivariate classification algorithms which involve the methods of Partial-Least Squares (PLS), Linear Discriminant Analysis (LDA) and Support Vector Machines (SVM). Partial-Least Squares (PLS) is a powerful regression method that decomposes an original set of descriptors representing a sample into a smaller set of variables. The method can also be seen as a transformation of the original data space into a new coordinate system with fewer dimensions. LDA methods attempt to find a linear transformation (discriminant function) between two variables which maximize the variance between groups and minimizes that within groups. SVM, as explained in Chapter 3, is a supervised learning method that maps a given dataset into a higher dimensional space where a maximal separating hyperplane is constructed to separate input data into groups. These statistical analysis methods have been applied in the analysis of spectroscopic data in prior studies.[45,109-113] We implement hybrid algorithms, involving combinations of the above methods and use them to classify FTIR spectra of cervical tissues. A leave-one out cross-validation procedure was used to validate our

algorithms. A lot of the past studies of tissue FTIR spectra used formalin-fixed paraffin embedded (FFPE) tissues. But it has been shown that formalin-fixed tissues are more suitable for IR spectra analysis, as they could better provide information pertaining to tissue biochemistry.[106] Hence, we use formalin-fixed tissues rather than FFPE tissues in this study.

5.2 Experiments

5.2.1 Materials and Methods

Formalin fixed-frozen cervical tissue samples were obtained and stored at -80^{0}C. Our tissue samples included that from cancerous sites of 18 patients who had been diagnosed with cervical cancer and sites from17 healthy (normal) volunteers. Our methods involved cutting 10μm microtome sections from the tissue samples. The microtome sections were placed on ZnSe windows and mounted in a sample holder for transmission analysis. Prior to each spectra collection, the sample chamber was purged with dry nitrogen so as to remove the interference of water vapor and CO_2 from the spectra. The background spectrum was collected on a ZnSe window without any tissue sample and a typical representation is shown in Figure 5.1. The peaks around 1600cm^{-1} and 3500cm^{-1} are attributed to water vapor absorption and the strong central peak at around 2300cm^{-1} is due to atmospheric CO_2. The spectra was obtained with a Thermo-Nicolet Nexus 670 FTIR spectrometer using signal averaging of 512 scans at a resolution of about 2 cm^{-1} in the range of 700 - 4000 cm^{-1} . Our spectra pre-processing included expansion, optional smoothing, water vapor correction and avoidable baseline correction.

Prior to any statistical analysis, all acquired spectra were normalized to peak intensity in the amide I region. This serves to eliminate any changes in intensity that may result from fluctuations in our section thickness. In our analysis, we utilized the fingerprint region of 900 -1750 cm^{-1}. An example spectrum for both the cancer and normal groups is shown in Figure 5.2.

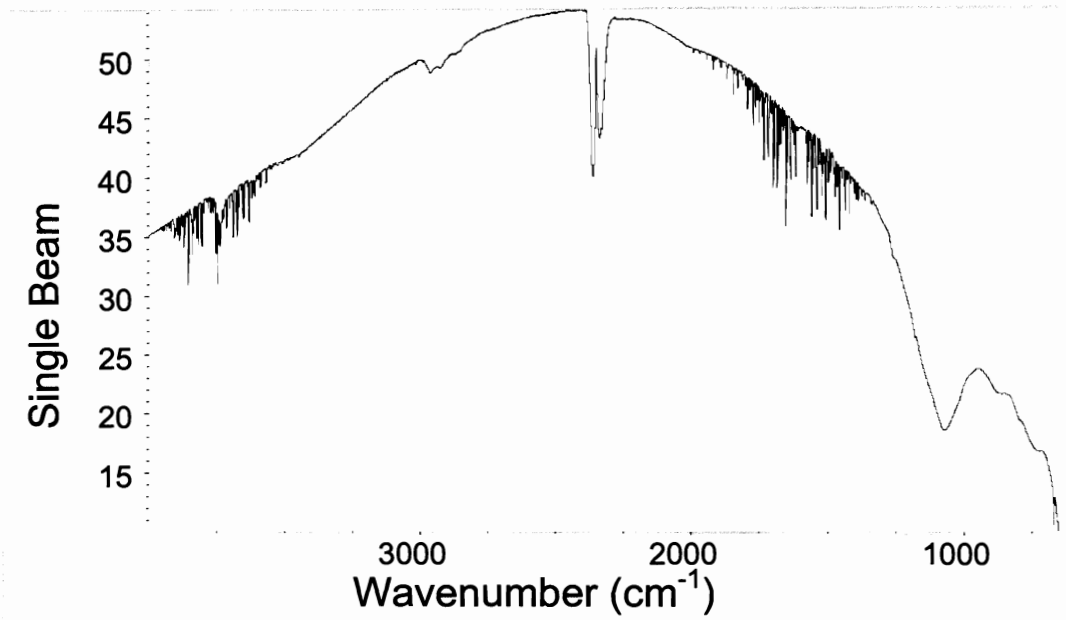

Figure 5.1- Typical single beam background spectrum collected from a ZnSe window. Peaks corresponding to atmospheric CO_2 and water absorption are observed and hence sample chamber is purged prior to collecting spectra from tissue.

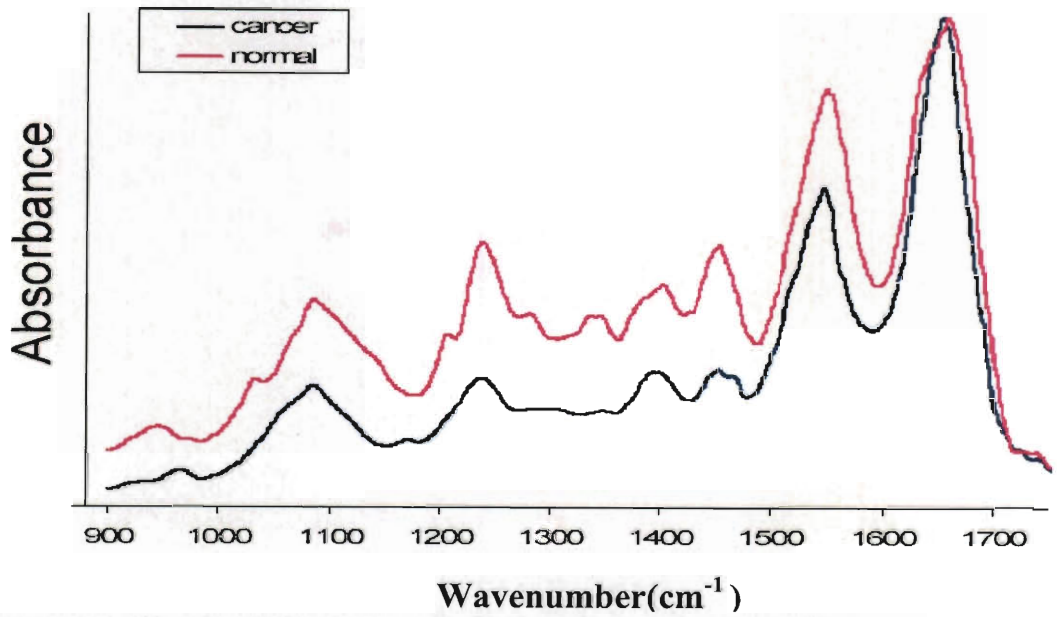

Figure 5.2- Example FTIR spectra for cancer and normal cervical tissue samples. Spectra are normalized to the peak intensity in the amide II band.

5.2.2 Statistical Analysis

After collecting the spectra, intensity ratios of the peaks of prominent bands were calculated, and their mean was compared for the cancer and normal groups. In calculating a ratio, the peak intensity value in the amide II band at around 1548 cm^{-1} was used as the denominator, and the peak value for any of the other bands was the numerator. Figure 5.3 shows the comparison of the mean intensity ratios between the groups. A 2-tailed t-test was used to test for statistically significant differences of the calculated ratios between the two groups. A p-value less than 0.05 was accepted as statistically significant. Multivariate algorithms involving PLS, SVM, and LDA were constructed for the classification of the tissue spectra. The PLS algorithm has as its input the intensity values over the entire wavelength region (900 -1750 cm^{-1}) of the FTIR absorption spectrum. It

decomposes the spectral representation (intensity at each wavelength point in the region considered) and represents it with scores from a few PLS components.

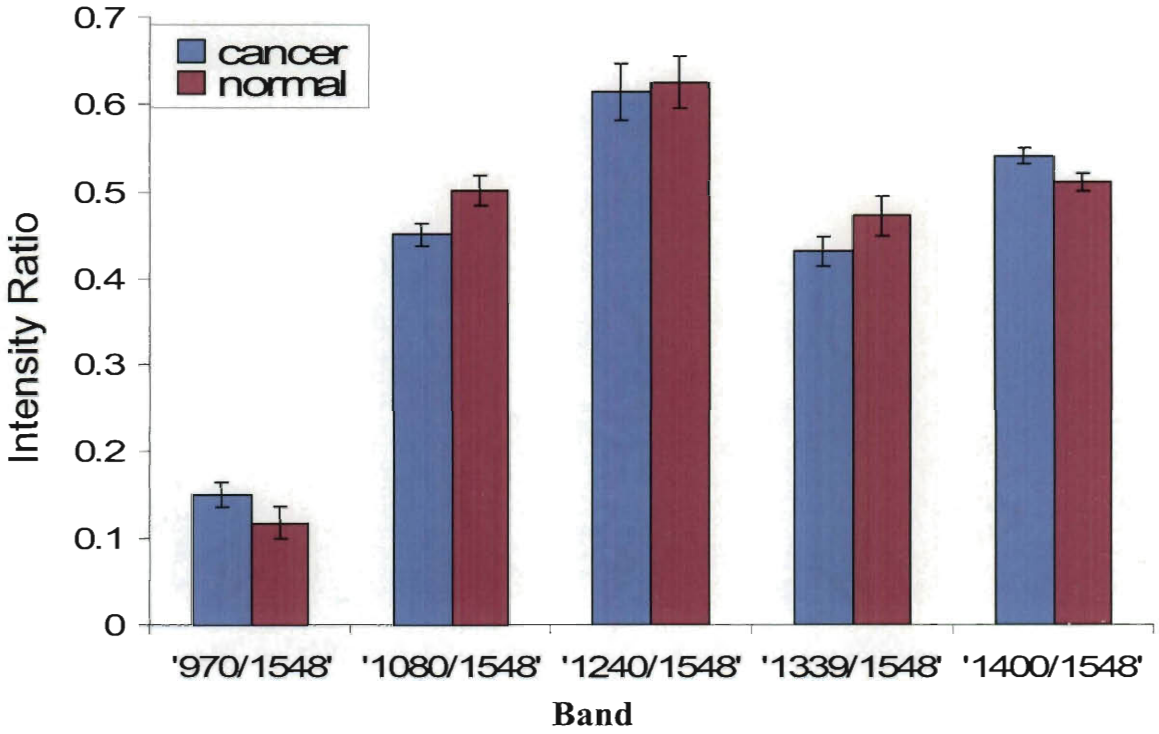

Figure 5.3- Mean intensity ratios of the different bands throughout the fingerprint region in the mid-IR are compared for the cancer and normal groups. A 2-tail t-test proved that the1080/1548 and the 1400/1548 ratios showed statistically significant differences between the two groups.

PLS is a dimension reduction technique that in constructing latent components includes information in the predictive variables as well as their data labels. So in this case, to arrive at the components, not only does PLS just seek variation in the intensity measurements, but it also takes into consideration, the corresponding label(or group) of each membership, for instance whether the measurement is from a cancerous or normal tissue. In this sense, PLS is a supervised learning method while PCA is unsupervised. Section 3.4.1 has more information on PLS and PCA methods. The absorption spectra

was normalized and mean-centered before being inputted into the PLS procedure. The root-mean-squared-error of cross validation (RMSECV) was used to validate the PLS procedure to determine the optimal number of components that characterize the model. For our data, the PLS algorithm selected scores from 5 principal components as an optimal representation for each measured spectrum. The scores were then transferred to a LDA and SVM algorithm to form the PLS-LDA and PLS-SVM classification algorithms respectively. A flowchart of the algorithm development process is depicted in Figure 5.4.

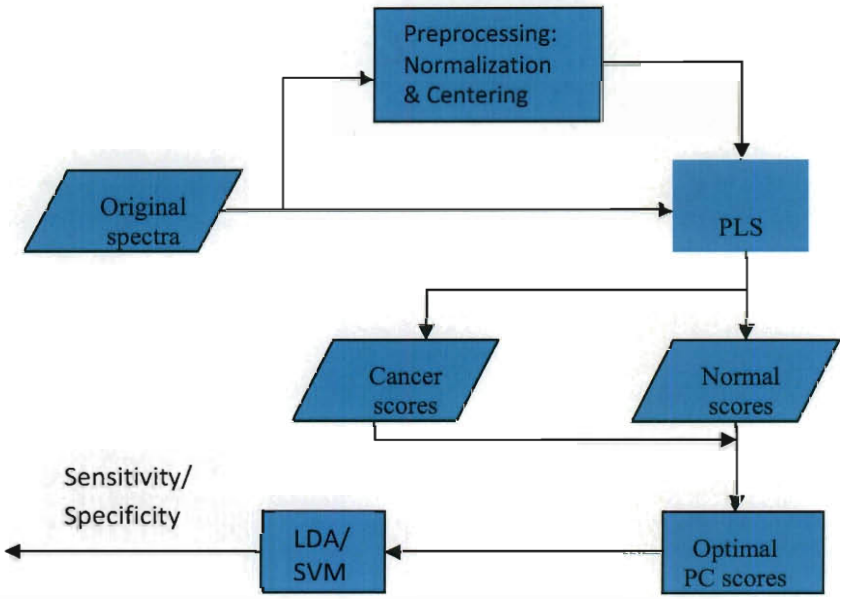

Figure 5.4- A flowchart of the algorithm development process.

A leave-one out cross-validation procedure was used to validate our PLS-LDA and PLS-SVM algorithms. Cross-validation is employed in testing classifiers when there are not enough samples to divide the dataset into a training/calibration set and a testing set. The premise is that the predictive ability of a model formed on part of a data (training set) can be tested out by how well it predicts the remainder of the data.[69] The idea of cross-validation, as mentioned in Chapter 3, involves dividing a dataset into p subsets and using

p-1 subsets to build a statistical model and testing this model on the left out subset. A total of p different models are built, each model excluding a unique subset (containing samples not included in training the model) to be tested.

5.3 Results and Discussion

Our results indicate that FTIR spectral analysis can access differences between the spectra of cancer and normal cervical tissues. A careful examination of Figure 5.2, which gives an example spectrum for the cancer and normal groups, indicates that, the differences in spectra are observed throughput the fingerprint region. The figure shows that The IR spectra of tissue in the fingerprint region is dominated by peaks in the amide I (around 1650 cm^{-1}) and amide II (around 1548 cm^{-1}) bands of proteins. The amide I peak results from a stretching motion of the C=O group whilst the amide II peak is mainly attributed to a coupled C—N stretching and a CNH deformation. The differences in the amide I and II bands between the cancer and normal groups were minimal. Table 5.1 summarizes contributions from some of the important tissue constituents that contribute to absorption in the mid-IR. A plot of the mean intensity ratios in Figure 5.3 shows the differences at peak intensity values of various bands in the spectra. The mean intensity values were calculated from the mean spectra of the cancer sites (comprising 47 measurements from the 18 cancerous samples) and the mean spectra of the normal sites (comprising 43 measurements from the 17 normal samples). We measured spectra from 2-4 sites of each tissue sample. A main contribution to the 1400 cm^{-1} band is from asymmetric and symmetric vibrational modes of methyl groups of protein.[98]

Absorption band (cm-1)	Corresponding biomolecules and their functional groups
1650	Amide I band arises from in plane C=O stretching vibration weakly coupled with C-N stretching and in plane N-H bending of the amide group in proteins
1540	Amide II band which arises from the N-H bending vibration strongly coupled to the C-N stretching vibration of protein
1400 and 1456	Symmetric and asymmetric CH_3 bending modes respectively of the methyl groups of proteins
1080	Symmetric phosphate PO^-_2 stretching modes (νsPO^-_2) of nucleic acid and the vibrational modes of collagen carbohydrate residues
1240	Asymmetric phosphate (PO^-_2) stretching modes ($\nu as\ PO^-_2$) of nucleic acids and the amide III/CH_2 wagging vibrations of collagen
1162	C-O stretching mode of the C-OH group of tyrosine residues and C-O groups of carbohydrates
1025	Vibrational modes of –CH2 OH groups and C-O stretching coupled with C-O bending of the C-OH groups of carbohydrates respectively
970	O-P–O antisymmetric stretching mode of DNA or to a phosphate monoester band of phosphorylated proteins and nucleic acids

Table 5.1- This shows some of the the vast number of biomolecules that contribute to FTIR absorption spectra of tissue in the mid-IR fingerprint region.

There was an increase in the peak intensity of this absorption band for the cancer group over the normal group. Less prominent protein peaks are also observed at the amide III peak (around 1240 cm^{-1}) which is mainly due to asymmetric phosphate PO^{-}_2 stretching modes of nucleic acids and the amide III/CH2 wagging vibrations in collagen.[114,115] The difference in the 1240/1548 intensity ratio wasn't statistically significant ($P > 0.05$). The difference in the 1080/1548 ratio was statistically significant between the two groups. The normal tissues had a greater absorption than the cancer tissues in the 1080 cm^{-1} band. This band primarily originates from symmetric phosphate PO^{-}_2 stretching modes ($vsPO^{-}_2$) of photodiester groups in nucleic acids and the vibrational modes of collagen residues.[98,114] The band at 970 cm^{-1} arises from phosphate monoester bands of nucleic acids and phosphorylated proteins. The changes between the cancer and normal groups are distributed throughout most of the fingerprint region of the absorption spectra, and univariate methods, such as intensity ratio analysis don't make full use of the entire absorption spectra. Hence, multivariate analysis involving PLS was applied to evaluate the data. Figure 5.5 depicts a cluster plot for the cancer and normal groups using PLS scores from two of the selected PLS components (PC5 vs. PC3). The PLS procedure couldn't fully differentiate all of the samples used in this study, as shown by an overlap between some of the points from the cluster of the normal group and some points from the cluster of the cancer group. Nonetheless, the algorithms developed, gave high sensitivity and specificity values as shown in Table 5.2. Both algorithms gave a sensitivity of 91% (43/47) and a specificity of 88% (38/43). This good classification results, which match that of other spectroscopy techniques, may suggest that the different spectral bands in the mid-IR region are diagnostically significant and that the exploration

of imaging systems using a few excitation wavelengths that belong to any of these bands for further tissue studies may yield important findings.

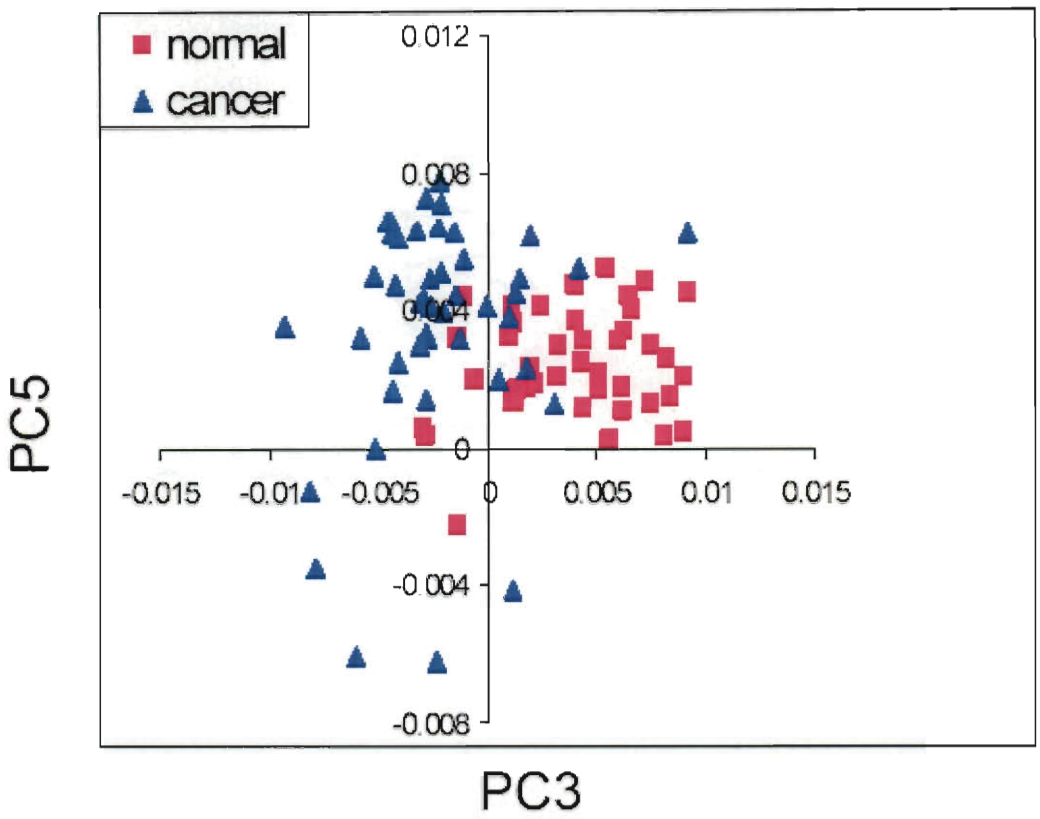

Figure 5.5- A plot depicting clusters of PLS scores for the normal and cancer groups. The data points in the plot are scores from two PLS components, PC3 and PC5.

	PLS-LDA	PLS-SVM
Sensitivity	91%	91%
Specificity	88%	88%

Table 5.2- Results of the algorithms in classifying between the normal and cancer tissue groups. The SVM classification produced the same results as the LDA classification.

5.4 CONCLUSION

In conclusion, we have examined the FTIR spectra of formalin-fixed frozen tissue sections of the cervix. We presented intensity ratio analysis of some of the pertinent absorption peaks and showed that there is significant variation between the spectra of normal and cancerous tissues throughout the fingerprint region. We further examined the differences between the spectra of the two groups by using the multivariate statistical analysis method of PLS. Two multivariate classification algorithms were then developed using scores from the PLS components. The algorithms were used to classify spectra into normal or cancer histopathological groups with high specificity and sensitivity values. The analysis methods we have used have made it possible to present a thorough study of the differences between the spectra of normal and cancerous tissues of the cervix. FTIR spectra analysis is very promising as an easy and fast method that may aid physicians in the diagnosis of cervical cancer.

Chapter 6: QCL based Mid-IR Imaging System

6.1 Introduction

Many tissue biochemical constituents have vibrational wavelengths in the fingerprint region (900 -1750 cm^{-1} (5.7-11μm)) of the mid- infrared(mid-IR) portion of the electromagnetic spectrum.[116,117] In Chapter 5 we presented FTIR spectroscopy work, that showed that absorption of the functional groups in some of the biomolecules vary significantly between the spectra of cancer and normal tissues of the cervix. As we noted in the chapter, many studies have found significant differences in the FTIR spectra, particularly in the fingerprint region, of normal and cancer tissues in other organs as well. In this chapter we present work on the development of a mid-IR imaging system that uses a quantum cascade laser (QCL) as an illumination source. The wavelength of the source, 9.53μm, was informed by the FTIR spectroscopy work which identified it as a possible diagnostically relevant wavelength that can distinguish between cancer and normal tissues. Some work has been done on the use of FTIR spectroscopic imaging technique for tissue studies.[105,118-123] This technique simply uses a focal plane array (FPA) in place of a single point detector and generated pseudo-color images that map pixel values to the detected intensity values to increase the contrast between the diseased and normal regions of tissue. The technique uses broadband light sources which are limited in power, spectral density and brightness which in turn limits the possible applicability of this in *in vivo* tissue studies. The use of laser sources that can deliver high spectral density and high brightness would be advantageous. Very few studies have been conducted on laser based mid-IR microscopy/imaging and even fewer have been concerned with investigation into

clinical diagnosis. Mid-IR optical coherence imaging has been developed for bio-engineered tissues,[124] mid-IR reflectance imaging has been demonstrated on chicken tissue and a transmission setup has been used to study celery tissue.[125,126] In this work, we have assembled a reflectance based imaging system that uses a continuous-wave QCL (cw-QCL) operating in the fingerprint region as a light source. When the reflectance imaging system is optimized in the future, it should be capable of the imaging of human tissues.

6.2 Background

The mid-IR region hasn't been widely explored for imaging due to the lack of appropriate light sources and enabling passive components.[127] The resolution for infrared (IR) microscopy is generally worse than that for visible light microscopy. Some of the contributing factors for this are the relatively low numerical apertures (NA) of the objectives, the higher wavelengths and the low brightness of conventional IR sources. QCLs are semiconductor laser sources of very high brightness which allow for sensitive detection of analytes.[125] The high brightness of QCLs, compared to more conventional sources, make them very suitable imaging sources. This advantage is very important for our intended application of tissue imaging in which we aim to explore biochemical and morphological contrast between normal and cancer tissues. Figure 6.1 depicts a graph showing FTIR absorption of cancerous breast tissues in the 900-1700 cm^{-1} (6-11μm) range. The figure illustrates that a wealth of spectral information can be accessed in the mid-IR region.

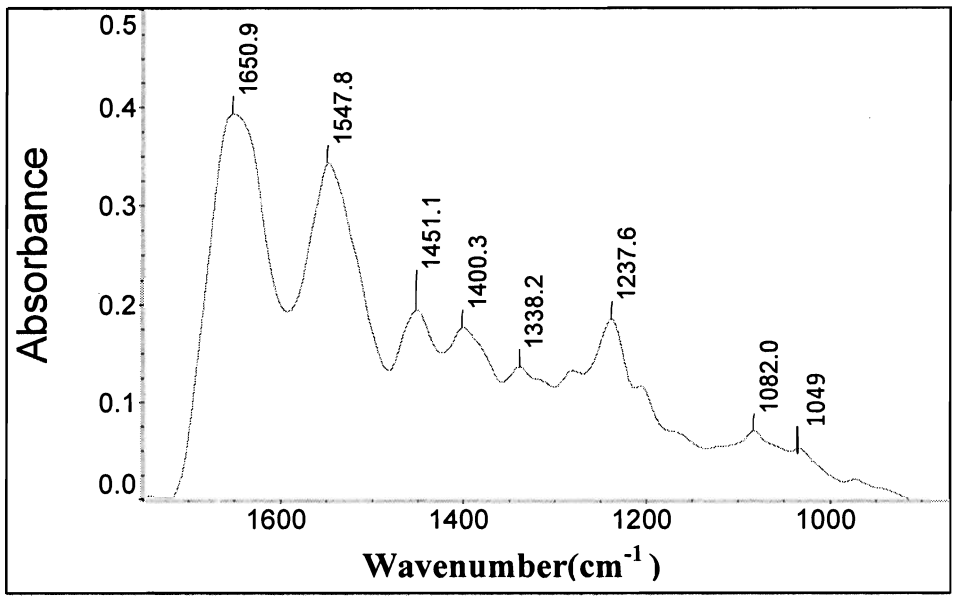

Figure 6.1- Representative FTIR spectrum for a breast tissue sample depicting functional groups of important tissue biomolecules.

The IR spectra of tissue is dominated by peaks in the amide I (around 1650 cm^{-1}) and amide II (around 1540 cm^{-1}) bands of proteins.[101,128,129] The amide I peak results from a stretching motion of the C=O group whilst the amide II peak is mainly attributed to a coupled C—N stretching and a CNH deformation. Weaker protein peaks are also observed at the amide III peak (around 1240 cm^{-1}) which is due to a coupled C—H / N—H deformation and a number of side-chain vibrations occur at around 1390 cm^{-1} and 1450 cm^{-1}.[129-131] All these bands are obvious in the collected spectrum in Figure 6.1. Also, it is very important to note that the presence of DNA contributes bands at around 1080 cm^{-1} , and around 1049 cm^{-1} which is attributed to the PO_2^- stretching vibrations of the phosphodiester backbone of nucleic acids. DNA also contributes to the peak at around 1240 cm.$^{-1}$[132,133] These DNA bands are important in the differentiation of carcinoma and normal tissues. The laser that we used has a wavelength of approximately 9.53μm (1049 cm^{-1}), which falls in a diagnostically significant absorption band of DNA.

6.3 System Setup

6.3.1 QCL Source

The QCL was thermoelectrically (TE) cooled since the system is designed to eventually be used system in a clinical setting. The QCL was mounted on a cold plate which is a TE cooler module (TE Technology Inc., CP-110) with capacity of 110W and we attached lug-mounted thermistor (TE Technology Inc., MP-2996) with resistance of 15KΩ to monitor the temperature of the plate. A graphene thermal pad was sandwiched between the laser and the plate to allow for efficient thermal contact and reliable heat conduction. Another thermistor (TE Technology Inc., MP-2379) was used to detect any excessive heating and trigger an alarm if overheating were to occur. The TE cooler has a fin and fun attached to its hot plate for heat dissipation and was powered by a 24V DC supply and controlled by a TE controller (TE Technology Inc., TC-48-20). This TE controller was set to operate in a cool-only-mode for the purposes of cooling down the cold plate and it regulates the cooler using pulse-width modulation. We applied thermal paste to the thermistors before attachment to the cold plate so as to allow for good thermal contact. We took further precautions to ensure that the temperature of the cold plate was close to the temperature of the sensor as much as possible since the TE controller measures the sensor temperature rather than the QCL attached cold plate which would be more ideal. These precautions included attaching the thermistor wires to the side of the cold plate with an aluminum tape to stimulate heat conduction around the wire. This is expected to minimize any temperature lag between the wire and the monitored temperature of the sensor head.[134] We wanted to be precise in monitoring the QCL

temperature so as to prevent any effects of temperature wavelength modulation of the device which in turn adds to a robust imaging system.

We generally operated the QCL between 1mW and 10mW of output power. A look at the L-I-V curve in Figure 6.2 makes it clear that even at the maximum output power of the laser (50mW), the heat load of the QCL per the equation P = I x V is P = 1.1 x 8= 8.8W is going to fall far short of the maximum capacity of the TE cooler. We operated the QCL at a room temperature and the measured ambient was never more than 3°C above this temperature.

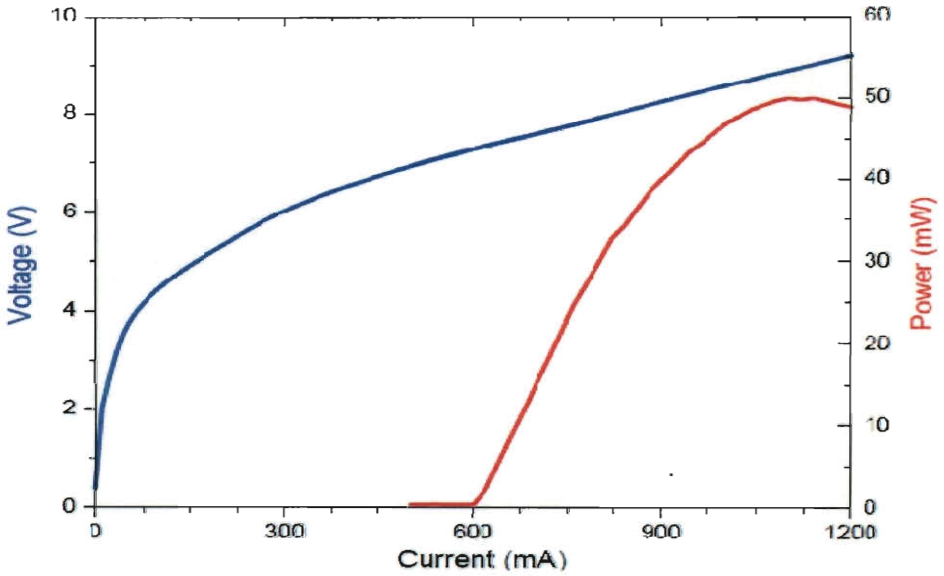

Figure 6.2- L-I-V characterization of the QCL laser source.

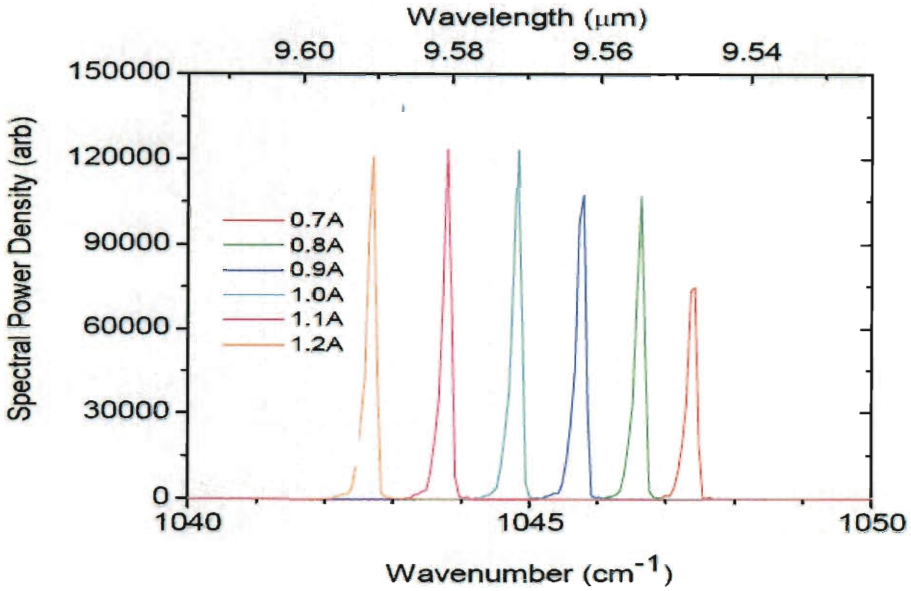

Figure 6.3- The emission spectrum of the QCL illumination source. This shows the spectral power density as a function of wavelength and operating current.

The cooling performance graph (not shown here) shows that at the operating temperature and the maximum measured ambient the cooling capacity of the TE cooler is around 110W hence stable and safe operation of the light source is expected. Figure 6.3 shows the emission spectrum of the QCL. It gives the spectral power density as a function of wavelength and operating current.

6.3.2 Reflectance Mode Setup

The system consists of the thermoelectrically cooled cw-QCL as the imaging source. Figure 6.4 depicts the simple microscope setup in reflectance mode. In the arrangement, the light beam impinges onto a collimator (ZnSe asphere) and made incident onto a 50:50 ZnSe beamsplitter. Either a ZnSe lens of focal length 12.7mm or BaF_2 lens of focal length 25mm is used interchangeably as L_1 for illumination and collection of reflected light from the sample. L_1 is used to achieve a magnification of

about 25x (All lenses have diameter of 25.4mm, have clear aperture of 0.9xdiameter and are from ISP Optics). The sample is on a translational stage controlled by LABVIEW. The back-reflected light from the sample is collected and focused onto a focal plane array (FPA) that is positioned in the image plane. The second lens, L_2 of focal length 25mm, when used in the setup, magnifies the image of L_1 to achieve a desired total magnification of around 80x. In selecting aspherics for the lenses, spherical aberration (assuming infinite conjugate) is negligible and a resolution of ~6.5μm for the objective may be achieved. This is at a cellular resolution level, and to obtain useful magnification, eliminating blurring effects, we designed the system not to exceed 80x magnification. The reflectance mode is investigated because it would be the configuration of choice for any potential *in-vivo* mid-IR imaging application.

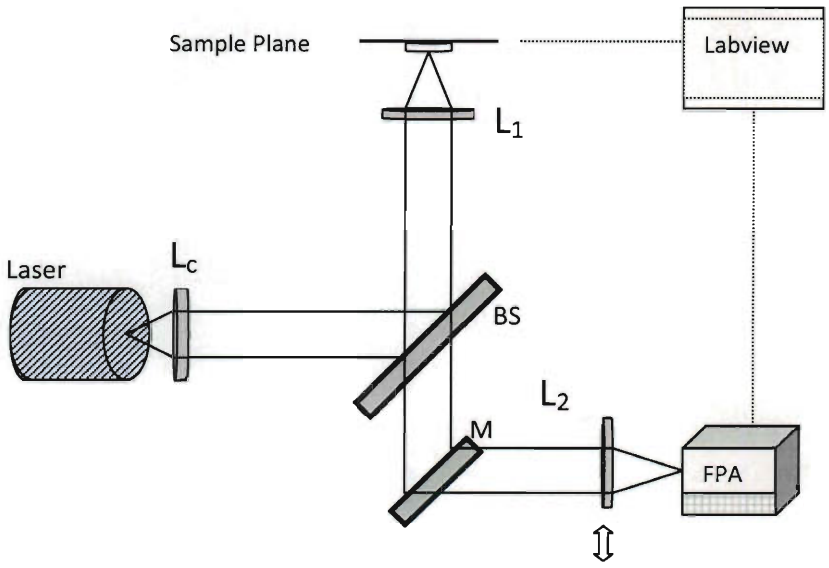

Figure 6.4- Microscopy setup for reflectance imaging of tissues. BS, Beamsplitter; L_1 objective lens stage, L_2 magnifying lens, L_c collimating lens, M mirror, FPA focal plane array detector.

The detector is a low cost FPA (Electrophysics Corp., PV-320L). It consists of uncooled ferroelectric sensors, with a broadband response range optimized for 8-14μm. The array resolution is 320 *240 pixels and the Noise-equivalent-power (NEP) is estimated to be ~3 x 10^{-9}W and has a pixel pitch of 48.5μm. The low spectral sensitivity of the camera limits the power of our QCL source to less than 10mW so as to prevent saturation. The use of a low cost high NEP detector underscores the fact that the microscopic system is cost-effective. Also, the detector didn't have to be cryogenically cooled like more sensitive detectors such as Mercury Cadmium Telluride (MCT) and this renders the system more viable for clinical applications.

6.3.3 Example Reflectance Images

We took images with reflectance mode setup of thin sections of celery tissue. About 20μm thickness of frozen celery tissue was cut, and placed flat onto a 2mm thick ZnSe slide. The slide was placed in a sample holder for imaging.

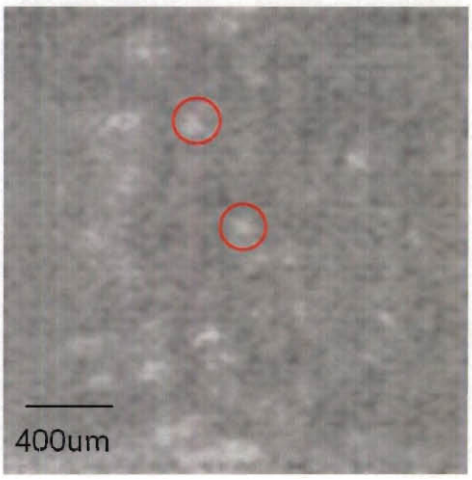

Figure 6.5- Imaging of celery tissue at 25x magnification.

Figure 6.5 is an image of a 20μm thin celery tissue. It should be noted that the image is acquired with a barium fluoride biconvex lens (NA of 0.45) which results in substantial diffraction loss and loss of resolution rather than the near diffraction limited performance that could be obtained from an aspherical ZnSe lens. Moreover, with a relatively small NA, the BaF_2 lens is substantially slow, hence the depth of field is longer and allows for an image to be registered on the camera with less fine-focusing than a faster lens. But the slower lens with smaller NA is going to result in considerably worse resolution. This accounts for our ability to get an image, but a blurred one using the BaF_2. Nonetheless tissue structures are visible as marked in red.

(a) (b)

Figure 6.6- (a) Interference pattern projected onto camera (b) USAF resolution target in reflectance mode at magnification of 25x.

QCLs are known to generally have higher divergence than other laser sources, but from our observation, this doesn't detract from its usefulness in imaging, since the use of a high NA lens can collect most of the light. We observed the Newton's ring interference pattern as shown in Figure 6.6(a). In Figure 6.6(b), the imaging of a USAF target in reflectance mode is presented. The target is made of patterned chromium bars on a glass substrate. The figure obtained at 25x is obtained after the IR beam is reflected off the chromium bars and a ZnSe lens with NA 0.9 serving as L_1, just as in Figure 6.4, but

without L_2, is used to image it onto the FPA. The bars are clearly visible and well resolved showing the feasibility of microscopic imaging at this wavelength. A camera with better NEP and detectivity would further improve the images considerably.

The gold standard for cancer diagnosis is biopsy, a surgical procedure to remove part of the cancer tissue, followed by histology, which involves extensive H&E staining and visible light microscopy to confirm the tissue pathology. Another procedure for diagnosis involves biopsy followed by immunohistochemistry which includes the labeling of tissue constituents such as proteins, lipids and carbohydrates with antibodies before microscopic examination. A mid-IR microscope has the advantage compared with the above methods, of not needing staining or antibody labeling for contrast but utilizing the intrinsic contrast provided by the absorption of proteins, lipids and carbohydrates under IR illumination. This clearly gives the mid-IR microscopy additional advantages of avoiding the cost of stains or antibodies and bypassing an additional system complexity of staining or antibody labeling. In the future, mid-IR coherent microscopy studies could add to the current understanding of the molecular basis of cancer as well as offer an alternative for the diagnosis of tissues.

6.4 Discussion and Conclusion

The FTIR absorption studies showed that the absorption of the functional groups of some compounds vary significantly for cancerous and normal tissues. Most of these absorptions occurred in the fingerprint region; this suggests that by using a QCL illumination source operating in the above region, we should be able to obtain contrasting images of biological relevance for diseased and normal tissues. Consequently we

designed and assembled a low cost, robust microscopic system which uses a high brightness QCL source operating at 9.53μm for illumination. In reflectance mode, an image of a USAF test target was acquired, and we imaged celery tissue as well. The tissue image wasn't very clearly resolved but further optimization and the use of cameras with better detectivity should produce better images. Such work could be explored in future studies. Our aim here was to describe work on the development of a reflectance based IR imaging system that utilize a mid-IR QCL operating in the fingerprint region as an illumination source. Such a system has the potential for diagnostic imaging of tissues. *In vivo* studies in organs such as the breast and the skin are especially promising in the field of mid-IR imaging. The skin is easily accessible and *in vivo* spectroscopy studies have been able to measure signals with remarkable SNR from it. Intensity variation in the hydration level of the skin has been measured as well as bands corresponding to glycerol and a host of other compounds. Triglycerol, in particular has been found to be in greater quantities in some normal tissues compared to cancerous tissues.[135] Additionally, recent studies suggest that the compound plays a role in signaling skin cells into reaching maturation; this signifies possible potential in helping people with ailments such as non-melanoma skin cancer and psoriasis which involve the abnormal proliferation and maturation in affected skin cells. FTIR spectroscopy using broadband sources has been useful in monitoring the concentration of these compounds; a high brightness source such as a QCL should be even more sensitive to small changes in the concentration of significant molecules. Hence, a novel concept worth implementing is infrared imaging or spectroscopy, with a QCL source in the attenuated total reflectance (ATR) mode for the diagnosis or treatment monitoring of non melanoma skin cancer.

Other organ sites that stand to benefit are the ones that are easily accessible via an endoscope such as the colon, esophagus and the gynecological sites of the cervix and the uterus. In these organs, a catheter can be passed down the channel of a silver halide probe to deliver air to the organ site which would reduce signatures of CO_2 and H_20 in the collected data. The use of silver halide probes in conjunction with the free space system we have assembled might hold the most promising path to eventual clinical applications.

The properties that make silver halide probes good candidates for *in vivo* imaging are that they are non toxic in biological tissues, have a broad spectral transmission in the mid-IR,[136] exhibit low attenuation, and are very flexible and hence can be coupled to an endoscope for imaging. The probes have already been very useful in FTIR spectroscopy for tissue diagnosis.[137-140] In an animal study by Katukuri *et al.*, they measured the FTIR spectra of dextran sulfate sodium(DSS) treated mice in the region of 950 - 1800cm^{-1}.[141] They found that important differences existed between the spectra of colitis and a control group and that the peaks at 1072, 1088 and 1740cm^{-1} had significant diagnostic potential, subsequently a PLS algorithm was developed to distinguish colitis and the control group with a sensitivity of 93% and a specificity of 88%. DSS is used to induce colitis in mice to serve as a representative experimental model for human inflammatory bowel disease.[142] In another study, *in vivo* spectroscopy work was conducted in the colon which revealed distinguishing characteristics between normal and cancerous tissues.[143] The FTIR spectra was collected with a ZnSe ATR crystal and it revealed that the relative intensity at the wavelengths of 1456cm^{-1} and 1413 cm^{-1} was less in normal tissues. Another important finding observed similarities between spectra collected noninvasively *in vivo* and that collected *in vitro*. Ring *et al.* measured the *in vivo* spectra of areas of the

skin including the forearm and lips with good signal to noise ratio with a silver halide probe coupled to a commercial FTIR instrument.[17] These studies provide evidence of the possibilities in *in vivo* mid-IR applications. Simple improvements and additions to the imaging system we have assembled would make it more ready for useful diagnostic applications in the future. An MCT FPA detector that is thermoelectrically cooled can be used for high sensitivity detection. With the commercial availability of room temperature operating QCLs that don't need any cooling, a very portable system for clinical use may be realized. Moreover, a widely tunable QCL can be used for illumination to allow for some flexibility in wavelength selection as well as the implementation of hyperspectral and multispectral imaging modalities to enhance contrast between diseased and normal tissues.

Chapter 7: Summary and Future Direction

7.1 Summary

In this thesis, we explored the application of spectroscopy techniques, new algorithms and imaging systems for the diagnosis of gynecological cancers. We conducted studies in mid-IR spectroscopy and imaging. We wanted to exploit the vast amount of molecules that have vibration frequencies in this region for spectroscopy to determine if it is possible to achieve good classifier performance. We measured the spectra of cervical tissues and developed classification algorithms for differentiating cancer from normal tissues. The performances of the algorithms were comparable to that of algorithms developed from UV-ViS optical spectroscopy. A wavelength in one of the significant bands in the spectra was selected and used as the excitation wavelength of a QCL-based mid-IR microscopic system. With further development in the future, this system should be viable for tissue studies and hopefully for accessing diagnostic information to aid in cancer diagnosis.

The UVC region has been mainly neglected in tissue spectroscopy due to the possibility of mutagenicity under the interrogation of UV rays. But studies have pointed to the fact that low levels of radiation are safe in humans. Given this fact, we trained an SVM algorithm on fluorescence spectra excited with UVC light, and we found that the classification performance of such an algorithm was comparable to other algorithms based on higher wavelengths of excitation. This suggests that this wavelength range has promising diagnostic potential.

We demonstrated the application of an SVM based classification algorithm for problems involving unbalanced datasets. These types of datasets can skew an algorithm's classification performance when trained in the conventional way for maximizing the overall accuracy. We demonstrated the training of an SVM algorithm which was trained subject to the Neyman Pearson criterion. In this case we constrained the sensitivity to have a high value while maximizing the specificity. Using this approach, fluorescence spectra of ovarian tissues were classified into different groups including that of cancer. This learning technique leads to fairly balanced classification results, that aren't skewed towards the group with the larger size.

We also assembled and demonstrated the cellular imaging capability of a needle-based high resolution reflectance fiber microscope. It is an inexpensive system that is developed for future biopsy applications using intrinsic tissue contrast.

Some improvements in our studies are warranted. The use of a large testing dataset withheld from training would give us a better idea of the generalization performance of the classifiers. Also, the development of classification algorithms to classify input data into groups involving precancerous lesions are much needed. For instance, in the FTIR classification of cervical data, a very useful outcome would be the ability to tell if a given patient has cervical dysplasia. Work also remains to be done on the reflectance fiber-mode microscope. We have demonstrated cellular imaging with this inexpensively developed system, but ultimately we need to perform *in vivo* testing of organ sites to determine its suitability for use in a clinical setting. Also, the use of multiple wavelengths to cover a wider region for mid-IR imaging is needed to elucidate

IR images, especially images of tissues. The use of cameras with better detectivity in the fingerprint region would also enhance image quality.

7.2 Future Direction

In the future, attempting a combination of FTIR and fluorescence spectroscopy to attempt to yield better classification results is warranted. Studies have reported the use of the combination of fluorescence, diffuse reflectance and light scattering spectroscopy methods, referred to as trimodal spectroscopy, to achieve better classification results than the use of any one of the techniques.[144] FTIR accesses the vibrational states of biomolecules while fluorescence spectroscopy depends on electronic transitions in molecules. If we combine these two spectroscopy techniques we get to access more properties of the different histopathological groups of tissues and may have a better chance of finding significant differences that would be diagnostic. Moreover, a combined imaging and spectroscopy system which uses the RFM to give visual cellular information and either the fluorescence or FTIR technique to provide detailed and broad spectral characteristics might yield an improvement in disease diagnosis.

Given the low prevalence of gynecological cancer diseases, we can still expect that the training of classification algorithms for binary classification is going to depend on some imbalance in the training data so research methods to address this are warranted. Alternative methods of dealing with imbalanced training sets, besides the NP criterion, should be studied and used in training spectroscopic data. Other classifiers besides SVM can also be studied with respect to the minimax, NP or other learning frameworks to determine which one provides the best needed results for cancer diagnosis. Also, novel

dimension reduction methods such as sparse PLS or sparse PCA may be explored for the analysis of optical spectroscopic data.

There is tremendous amount of knowledge about tissue biochemistry that can be accessed in the mid-IR due to the fact that molecular vibrations occur on the order of wavelengths in this region. There is significant tissue absorption in this region, but on the other hand there is also low scattering. This can open up applications in coherent imaging especially with high brightness sources. With the vast amount of molecules that vibrate in the mid-IR, applications such as imaging using intrinsic contrast provided by the tissue constituents rather than the use of any expensive dyes are viable clinically. A lot of studies have shown the *ex vivo* diagnosis of tissue using intrinsic contrast and pseudo-color images. With the recent advances in the development of portable light sources such as the QCL and silver halide fibers, one can envision spectroscopy and imaging systems that can probe tissue *in vivo* for relevant diagnostic information. In the future, a tunable mid-IR laser with a flexible silver halide probe that exhibit very low attenuation may be used to image bulk tissues via the ATR configuration. Subsequently, tissue contrast studies of true color and false color images of cancerous and normal tissues may be performed to further explore the clinical potential of the mid-IR region.

References

1. A. S. Ross, A. Noffsinger and I. Waxman, "Narrow band imaging directed EMR for Barrett's esophagus with high-grade dysplasia," *Gastrointestinal Endoscopy* (65)1, 166-169 (2007)

2. K. Gono, T. Obi, M. Yamaguchi, N Ohyama, H. Machida, Y. Sano, S. Yoshida, Y. Hamamoto and T. Endo, "Appearance of enhanced tissue features in narrow-band endoscopic imaging," *J. Biomed. Opt.* 9, 568–577 (2004)

3. K. Gono, M. Yamaguchi, and N. Ohyama, "Improvement of image quality of the electroendoscope by narrowing spectral shapes of observation light," In Proceedings of the International Congress of Imaging Science, Imaging Society of Japan, 399–400 (2002)

4. B. A. Flusberg, E.D. Cocker, W. Piyawattanametha, J. C. Jung, E.L.M. Cheung and M.J. Schnitzer "Fiber-optic fluorescence imaging," *Nature Methods* 2, 941–950 (2005)

5. T. Ota, H. Fukuyama , Y. Ishihara, H. Tanaka, and T. Takamatsu, "*In situ* fluorescence imaging of organs through compact scanning head for confocal laser microscopy," *J. Biomed. Opt.* 10, 024010 (2005)

6. P.M. Delaney, R.G. King, J.R. Lambert and M.R. Harris, "Fibre optic confocal imaging (FOCI) for subsurface microscopy of the colon *in vivo*," *J. Anat.* 184, 157–160 (1994)

7. A. L. Polglase, W. J. McLaren, S. A. Skinner, R. Kiesslich, M. F. Neurath, and P. M. Delaney, "A fluorescence confocal endomicroscope for in vivo microscopy of the upper- and the lower-GI tract," *Gastrointest. Endosc.* 62, 686–695 (2005)

8. L.D. Swindle, S.G. Thomas, M. Freeman and P.M. Delaney, "View of Normal Human Skin In Vivo as Observed Using Fluorescent Fiber-Optic Confocal Microscopic Imaging," *Journal of Investigative Dermatology* 121, 706–712 (2003)

9. M. Rajadhyaksha and S. Gonzalez, "Real-time in vivo confocal fuorescence microscopy," In:Myeck MA, Pogue B, (eds). Handbook of Biomedical Fluorescence. New York:Dekker, 143-179 (2003)

10. B. Mayinger, P. Horner, M. Jordan, C. Gerlach, T. Horbach, W. Hohenberger and E.G. Hahn, "Light-induced autofluorescence spectroscopy for the endoscopic detection of esophageal cancer," *Gastrointest Endosc* 54, 195–201(2001)

11. N. Uedo, H. Iishi, M. Tatsuta, T. Yamada, H. Ogiyama, K. Imanaka, N. Sugimoto, K. Higashino, R. Ishihara, H. Narahara, and S. Ishiguro, "A novel videoendoscopy system by using autofluorescence and reflectance imaging for diagnosis of esophagogastric cancers," *Gastrointest. Endosc.* 62, 521–528 (2005)

12. G. McConnell and E. Riis, "Two-photon laser scanning fluorescence microscopy using photonic crystal fiber," *J. Biomed. Opt.* 9(5), 922 - 927 (2004)

13. D. Kim, K.H. Kim, S. Yazdanfar and P.T.C. So "Optical biopsy in high-speed handheld miniaturized multifocal multiphoton microscopy," *Proceedings of SPIE* 5700, 14–22 (2005).

14. W. Yicong, X. Jiefeng, C. Yongping, M.J. Cobb, L. Min-Jun and L. Xingde, "Fiber-optic endomicroscopy for intrinsic two-photon fluorescence imaging of epithelial cells and tissues," in Conference on Lasers and Electro-Optics(CLEO), 1-2, June (2009)

15. G. J. Tearney, S. A. Boppart, B. E. Bouma, M. E. Brezinski, N. J. Weissman, J. F. Southern, and J. G. Fujimoto, "Scanning single-mode fiber optic catheter–endoscope for optical coherence tomography," *Opt. Lett.* 21(7), 543-545 (1996)

16. C. Kendall, N. Stone, N. Shepherd, K. Geboes, B. Warren, R. Bennett and H. Barr "Raman spectroscopy, a potential tool for the objective identification and classification of neoplasia in Barrett's oesophagus," *J Pathol.* 200, 602–609 (2003)

17. A. Ring, V. Schreiner, H. Wenck, K. P. Wittern, L. Ku and R. Keyhani "Mid-infrared spectroscopy on skin using a silver halide fibre probe in vivo," *Skin Research and Technology* 12, 18–23(2006)

18. T. J. Muldoon, S. Anandasabapathy, D. Maru, and R. Richards-Kortum, "High-resolution imaging in Barrett's esophagus: a novel, low-cost endoscopic microscope," *Gastrointestinal Endoscopy* 68, 737-744 (2008)

19. T. J. Muldoon, N. Thekkek, D. Roblyer, D. Maru, N. Harpaz, J. Potack, S. Anandasabapathy, and R. Richards-Kortum, "Evaluation of quantitative image analysis criteria for the high-resolution microendoscopic detection of neoplasia in Barrett's esophagus," *J. Biomed. Opt.* 15, 026027 (2010)

20. J. Sun, C. Shu, B. Appiah and R. Drezek, "Needle-compatible single fiber bundle image guide reflectance endoscope," *J Biomed. Opt.* 15, 040502 (2010)

21. Centers for Disease Control and Prevention (CDC), "Schematic drawing of female reproductive organs" Wikipedia 6 April 2008, 17 September 2010 <http://en.wikipedia.org/wiki/File:Scheme_female_reproductive_system-en.svg>

22. National Cancer Institute(NCI), "Ovarian Epithelial Tumors Traced to Fallopian Tubes", 14 August 2010 <http://www.cancer.gov/cancertopics/causes/ovarian/disease-source0408>

23. M.A. Rossing, K.G. Wicklund, K.L. Cushing-Haugen and N.S. Weiss "Predictive value of symptoms for early detection of ovarian cancer" *J. Natl Cancer Inst.*102, 222–229 (2010)

24. National Cancer Institute(NCI), "BRCA1 and BRCA2: Cancer Risk and Genetic Testing" 29 may 2009, 12 August 2010 <http://www.cancer.gov/cancertopics/factsheet/Risk/BRCA>

25. I. Cass and B.Y. Karlan, "Ovarian Cancer Symptoms Speak Out—But What Are They Really Saying?" *J. Natl. Cancer Inst.* 102 (4), 211-212(2010)

26. National Cancer Institute(NCI), "Cervical Cancer" 12 August 2010 <http://www.cancer.gov/cancertopics/types/cervical>

27. National Cancer Institute(NCI), "Human Papillomaviruses and Cancer" 12 August 2010 < http://www.cancer.gov/cancertopics/factsheet/Risk/HPV>

28. R. Sankaranarayanan, R. Wesley, T. Somanathan, N. Dhakad, B. Shyamalakumary, N.S. Amma, D.M. Parkin and M.K. Nair, "Visual inspection of the uterine cervix

after the application of acetic acid in the detection of cervical carcinoma and its precursors," *Cancer* 83, 2150–2156 (1998)

29. P.D. Blumenthal, L. Gaffikin, Z.M. Chirenje, J. McGrath, S. Womack and K. Shah, "Adjunctive testing for cervical cancer in low resource settings with visual inspection, HPV, and the Pap smear," *International Journal of Gynecology & Obstetrics*72(1), 47-53 (2001)

30. D.C. McCrory, D.B. Matchar, L. Bastain, S. Datta, V. Hasselblad, J. Hickey, E. Myers and K. Nanda "Evaluation of cervical cytology," Evidence Report/Technology Assessment No. 5. AHCPR Publication No. 99-E010. Rockville (MD): Agency for Health Care Policy and Research; February (1999)

31. Food and Drug Administration(FDA), "Re: P0202 Thinprep Imaging System", 3 September 2010 <http://www.accessdata.fda.gov/cdrh_docs/pdf2/P020002a.pdf>

32. B. Appiah, M. Davenport, M. Michaelides, V. Nammalvar, Urs Utzinger and R. Drezek, "Application of the Neyman Pearson criterion to ovarian cancer fluorescence diagnosis,"*Manuscript to be submitted* (2010)

33. American Cancer Society, "Ovarian Cancer Overview" 14 august 2010 <http://www.cancer.org/cancer/ovariancancer/overviewguide/ovarian-cancer-overview-key-statistics>

34. National Cancer Institute(NCI), "SEER Stat Fact Sheets: Ovary" 14 August 2010 <http://seer.cancer.gov/statfacts/html/ovary.html#risk>

35. M.F. Mitchell, S.B. Cantor, C. Brookner, U. Utzinger, D. Schottenfeld and R. Richards-Kortum, "Screening for squamous intraepithelial lesions with fluorescence spectroscopy," *Obstet. Gynecol.* 94(5), 889–896 (1999)

36. N. Ramanujam, M.F. Mitchell, A. Mahadevan, S. Thomsen, E. Silva and R. Richards-kortum, "Fluorescence spectroscopy—a diagnostic-tool for cervical intraepithelial neoplasia (Cin)," *Gynecol. Oncol.* 52(1), 31–38 (1994)

37. N. Ramanujam, M.F. Mitchell, A. Mahadevan, S. Thomsen, A. Malpica and T. Wright, N. Atkinson and R. Richards-Kortum, "Spectroscopic diagnosis of cervical intraepithelial neoplasia (CIN) in vivo using laser-induced fluorescence spectra at multiple excitation wavelengths," *Lasers Surg. Med.* 19(1), 63–74 (1996)

38. S.K. Chang, M. Follen, A. Malpica, U. Utzinger, G. Staerkel, D. Cox, E. Neely Atkinson, C. MacAulay and R. Richards-Kortum, "Optimal excitation wavelengths for discrimination of cervical neoplasia," *IEEE Trans. Biomed. Eng.* 49 (10), 1102–1111 (2002)

39. P.K. Gupta, S.K. Majumder and A. Uppal. "Breast cancer diagnosis using N2 laser excited autofluorescence spectroscopy," *Lasers Surg. Med.* 21, 417–422 (1997)

40. R. A. Schwarz, W. Gao, C. R. Weber, C. Kurachi, J.J. Lee, A. K. El-Naggar, R.R. Kortum and A. M. Gillenwater, "Noninvasive Evaluation of Oral Lesions Using Depth-sensitive Optical Spectroscopy," *Cancer* 115, 1669-79 (2009)

41. Y. Yang, G.C. Tang, M. Bessler and RR. Alfano. "Fluorescence spectroscopy as a photonic pathology method for detecting colon cancer," *Lasers Life Sci.* 6(4), 259–276 (1995)

42. C.Y. Wang, Lin JK, Chen BF, Chiang HK. "Autofluorescence spectroscopic differentiation between normal and cancerous colorectal tissues by means of a two-peak ratio algorithm," *J Formos Med Assoc.* 98(12), 837-43 (1999)

43. D. Zaak, H. Stepp, R. Baumgartner, P. Schneede, R. Waidelich, D. Frimberger, A. Hartmann, R. Künchel, A. Hofstetter and A. Hohla, "Ultraviolet-excited (308 nm) autofluorescence for bladder cancer detection," *Urology* 60(6), 1029-33 (2002)

44. C. Redden Weber, R.A. Schwarz, E.N. Atkinson, D.D. Cox, C. Macaulay, M. Follen, and R. Richards-Kortum "Model-based analysis of reflectance and fluorescence spectra for in vivo detection of cervical dysplasia and cancer," *J. Biomed Opt.* 13, 064016 (2008)

45. C. Zhu, G.M. Palmer, T.M. Breslin, J. Harter and N. Ramanujam, "Diagnosis of Breast Cancer Using Diffuse Reflectance Spectroscopy: Comparison of a Monte Carlo versus Partial Least Squares Analysis Based Feature Extraction Technique," *Lasers Surg. Med.* 38(7), 714-24 (2006)

46. P. Diagaradjane, M.A. Yaseen, J. Yu, M.S. Wong and B. Anvari, "Synchronous fluorescence spectroscopic characterization of DMBA-TPA-induced squamous cell carcinoma in mice," *J. Biomed. Opt.* 11(1), 014012 (2006)

47. P.V. Butte, B.K. Pikul, A. Hever, W.H. Yong, K.L. Black, L. Marcu, "Diagnosis of meningioma by time-resolved fluorescence spectroscopy" *J Biomed Opt.* 10(6), 064026 (2005)

48. H.J. van Staveren, R.L. van Veen, O.C. Speelman, M.J. Witjes, W.M. Star and J.L. Roodenburg, "Classification of clinical autofluorescence spectra of oral

leukoplakia using an artificial neural network: A pilot study," *Oral Oncol.* 36(3), 286–29 (2000)

49. S.D. Kamath, R.A. Bhat, S. Ray and K.K. Mahato "Autofluorescence of normal, benign, and malignant ovarian tissues: a pilot study," *Photomedicine and Laser Surgery* 27(2), 325-35 (2009)
50. S. D. Kamath and K.K. Mahato "Principal Component Analysis (PCA)-Based k-Nearest Neighbor (k-NN) Analysis of Colonic Mucosal Tissue Fluorescence Spectra," *Photomedicine and Laser Surgery* 27(4), 659-668 (2009)
51. M. Chandra, J. Scheiman, D. Simeone, B. McKenna, J. Purdy, and M.A. Mycek, "Spectral areas and ratios classifier algorithm for pancreatic tissue classification using optical spectroscopy," *J. Biomed. Opt.* 15(1), 010514 (2010)
52. G.S. Nayak, S. Kamath, K.M. Pai, A. Sarkar, S. Ray, J. Kurien, L. D'Almeida, B.R. Krishnanand, C. Santhosh, V.B. Kartha and K.K. Mahato, "Principal component analysis and artificial neural network analysis of oral tissue fluorescence spectra: Classification of normal premalignant and malignant pathological conditions," *Biopolymers* 82, 152–166 (2006)
53. U. Utzinger, M. Brewer, E. Silva, D. Gershenson, R. C. Blast Jr., M. Follen, and R. Richards-Kortum, "Reflectance spectroscopy for in vivo characterization of ovarian tissue," *Lasers Surg. Med.* 28, 56–66 (2001)
54. M. Brewer, U. Utzinger, J.K. Barton, J.B. Hoying, N.D. Kirkpatrick, W.R. Brands, J.R. Davis, K. Hunt, S.J. Steven and F.G. Arthur, "Imaging of the ovary," *Technology in Cancer Research & Treatment* 3(6), 617-627 (2004)

55. M. Brewer, U. Utzinger, E. Silva, D. Gershenson, R.C. Blast, M. Follen and R. Richards-Kortum, "Fluorescence spectroscopy for *in vivo* characterization of ovarian tissue," *Lasers Surg. Med.* 29, 128-135 (2001)

56. A.A. Tanbakuchi, J.A. Udovich, A.R. Rouse, K.D. Hatch and A.F. Gmitro, "In vivo imaging of ovarian tissue using a novel confocal microlaparoscope," *American Journal of Obstetrics and Gynecology*, 202(1):90.e1-90.e9 (2010)

57. C. Zhu, E.S. Burnside, G.A. Sisney, L.R. Salkowski, J.M. Harter, B. Yu, and N. Ramanujam, "Fluorescence Spectroscopy: An Adjunct Diagnostic Tool to Image-Guided Core Needle Biopsy of the Breast," *IEEE Trans. Biomed. Eng.* 56(10), 2518–2528 (2009)

58. C. Zhu, G.M. Palmer, T.M. Breslin, J. Harter and N. Ramanujam, "Diagnosis of breast cancer using fluorescence and diffuse reflectance spectroscopy: a Monte-Carlo-model-based approach," *J. Biomed. Opt.* 13, 034015 (2008)

59. G.M. Palmer, C. Zhu, T.M. Breslin, F. Xu, K.W. Gilchrist, and N. Ramanujam, "Monte Carlo-based inverse model for calculating tissue optical properties. Part II: Application to breast cancer diagnosis," *Appl. Opt.* 45, 1072-1078 (2006)

60. S.K. Majumder, N. Ghosh and P.K. Gupta, "Support vector machine for optical diagnosis of cancer" *J. Biomed. Opt.* 10, 024034 (2005)

61. M. Bonneville, J. Meunier, Y. Bengio, and J. P. Soucy, "Support vector machines for improving the classification of brain pet images," *Proc. SPIE* 3338, 264–273 (1998)

62. M.A. Davenport, R.G. Baraniuk, and C.D. Scott, "Tuning support vector machines for minimax and Neyman-Pearson classification," *IEEE Trans. on Pattern Analysis and Machine Intelligence* 32(10), 1888-1898 (2010)

63. C. Scott and R. Nowak, "A Neyman-Pearson approach to statistical learning," *IEEE Trans. on Information Theory* 51(11), 3806-3819 (2005)

64. M.A. Davenport, R.G. Baraniuk, and C.D. Scott, " Controlling False Alarms With Support Vector Machines," in Proc. IEEE International Conf. Acoustics, Speech, and Signal Processing, (2006)

65. C. Y. Wang, C. T. Chen, C. P. Chiang, S. T. Young, S. N. Chow and H. K. Chiang, "A probability-based Multivariate Statistical Algorithm for Autofluorescence Spectroscopic Identification of Oral Carcinogenesis," *Photochem. Photobiol.* 69, 471-477 (1999)

66. C. Zhu, T.M. Breslin, J. Harter and N. Ramanujam "Model based and empirical spectral analysis for the diagnosis of breast cancer," *Opt Express.* 16, 14961–14978 (2008)

67. Statsoft, "Partial Least Squares (PLS)" 18 August 2010, http://www.statsoft.com/textbook/partial-least-squares/

68. P. Geladi and B. Kowalski, "Partial least-squares regression: a tutorial" *Analytica Chimica Acta* 185, 1-17(1986)

69. R.G. Brereton, "Introduction to multivariate calibration in analytical chemistry," *Analyst* 125, 2125-2154 (2000)

70. JSU Hjorth, "Computer intensive statistical methods: Validation, model selection, and bootstrap," London, New York: Chapman & Hall (1994)

71. T. Hastie, R. Tibshirani, J. Friedman, Model assessment and selection. In: Hastie T, Tibshirani R, Friedman J, editors. *The elements of statistical learning*. New York: Springer; 193-224, (2001)

72. R.O. P. Draga, M.C. M. Grimbergen, P.L. M. Vijverberg, C.F. P. van Swol, T.G.N. Jonges, J.A. Kummer and J. L. H. Ruud Bosch "In Vivo Bladder Cancer Diagnosis by High-Volume Raman Spectroscopy," *Analytical Chemistry* 82 (14), 5993-5999 (2010)

73. R. Richards-Kortum and E Sevick-Muraca "Quantitative optical spectroscopy for tissue diagnosis," *Annual Review of Physical Chemistry* 47, 555-606 (1996)

74. J.R. Lakowicz "*Principles of Fluorescence Spectroscopy.*" New York:Plenum (1985)

75. N. Ramanujam, M. Mitchell, A. Mahadevan, S. Warren, S. Thomsen, E. Silva and R. Richards-Kortum, "In vivo diagnosis of cervical intraepithelial neoplasia using 337-nm excited laser-induced fluorescence," *Proceedings of the National Academy of Science* 91, 10193-10197 (1994)

76. K. T. Schomacker, J. K. Frisoli, C. C. Compton, T. J. Flotte, J. M. Richter, N. S. Nishioka and T. F. Deutsch, "Ultraviolet laser-induced fluorescence of colonic tissue: basic biology and diagnostic potential," *Lasers Surg. Med.* 12, 63-78 (1992)

77. I. Georgakoudi, B.C. Jacobson, M.G. Muller, E.E. Sheets, K. Badizadegan, D.L. Carr-Locke, C.P. Crum, C.W. Boone, R.R. Dasari, J. Van Dam and M.S. Feld, "NAD(P)H and collagen as in vivo quantitative fluorescent biomarkers of epithelial precancerous changes," *Cancer Res.* 62,682 – 687 (2002)

78. L. Brancaleon, A.J. Durkin, J.H. Tu, G. Menaker, J.D. Fallon and N. Kollias, "In vivo fluorescence spectroscopy of nonmelanoma skin cancer," *Photochem. Photobiol.* 73, 178-183 (2001)

79. Y. Yang, A. Katz, E.J. Celmer, M. Zurawska-Szczepaniak, and R.R. Alfano, "Fundamental Differences of Excitation Spectrum Between Malignant and Benign Breast Tissues," *Photochemistry and Photobiology* 66, 518-522 (1997)

80. N. Kollias, R. Gillies, M. Moran, I.E. Kochever, and R.R. Anderson, "Endogenous Skin Fluorescence Includes Bands that May Serve as Quantitative Markers of Aging and Photoaging," *Journal of Investigative Dermatology* 111, 776-780 (1998)

81. Food and Drug Administration(FDA), "Guidance for Industry Electro-optical Sensors for the In VivoDetection of Cervical Cancer and its Precursors:", 25 August 2010 <http://www.fda.gov/OHRMS/DOCKETS/98fr/992211gd.pdf>

82. K. Sokolov, M. Follen and R. Richards-Kortum, "Optical spectroscopy for detection of neoplasia," *Curr. Opin. Chem. Biol.* 6(5), 651–658 (2002)

83. Food and Drug Administration (FDA), "Device Approval and Clearances"25 August 2010 <http://www.fda.gov/MedicalDevices/ProductsandMedicalProcedures/DeviceApprovalsandClearances/default.htm >

84. Spectra Science, 11 September 2010 http://www.spectrascience.com

85. A. Staylor, "GI Endoscopy: Thriving on Innovation," Medtech Insight A#2010400048, June (2010)

86. C. Liang, M. Descour, K. B. Sun, and R. Richards-Kortum, "Fiber confocal reflectance microscope (FCRM) for in-vivo imaging," *Opt. Express* 9, 821-830

(2001)

87. S. Yoshida, S. Tanaka, M. Hirata, R. Mouri, I. Kaneko, S. Oka, M. Yoshihara and K. Chayama, "Optical biopsy of GI lesions by reflectance-type laser-scanning confocal microscopy," *Gastrointest. Endosc.* 66, 144-149 (2007)
88. K. C. Maitland, A. M. Gillenwater, M. D. Williams, A. K. El-Naggar, M. R. Descour and R. R. Richards-Kortum, "In vivo imaging of oral neoplasia using a miniaturized fiber optic confocal reflectance microscope," *Oral Oncol.* 44, 1059-1066 (2008)
89. A. F. Gmitro and D. J. Aziz, "Confocal microscopy through a fiber-optic imaging bundle," *Opt. Lett.* 18, 565-567 (1993)
90. F. Jean, G. Bourg-Heckly and B. Viellerobe, "Fibered confocal spectroscopy and multicolor imaging system for in vivo fluorescence analysis," *Opt. Express* 15, 4008-4017 (2007)
91. R. Juskaitis, T. Wilson and T. F. Watson, "Real-time white light reflection confocal microscopy using a fiber-optic bundle," *Scanning* 19, 15-19 (1997)
92. V. Dubaj, A. Mazzolini, A. Wood, and M. Harris, "Optic fiber bundle contact imaging probe employing a laser scanning confocal microscope," *J. Microsc.* 207, 108-117 (2002)
93. R. Kiesslich, M. Goetz, M. Vieth, P. R. Galle, and M. F. Neurath, "Technology Insight: confocal laser endoscopy for in vivo diagnosis of colorectal cancer," *Nat. Clin. Pract. Oncol.* 4, 480-490 (2007)
94. T. J. Muldoon, M. C. Pierce, D. L. Nida, M. D. Williams, A. Gillenwater, and R. Richards-Kortum, "Subcellular-resolution molecular imaging within living tissue

by fiber microendoscopy," *Opt. Express* 15, 16413-16423 (2007)

95. Sumitomo Electric, "Silica image guide for fiberscope," Proprietary Technical Document (2008)

96. A. G. von Arnim, X. W. Deng, and M. G. Stacey, "Cloning vectors for the expression of green fluorescent protein fusion proteins in transgenic plants," *Gene* 221, 35-43 (1998)

97. B. Appiah, V. Nammalvar and R. Drezek, "Statistical analysis of FTIR spectra of cervical tissues and diagnostic algorithms for cervical cancer," *Proc. SPIE* 6863, 68630V (2008)

98. S. Neviliappan, L. Fang Kan, T. Tiang Lee Walter, S. Arulkumaran and P.T. Wong, "Infrared spectral features of exfoliated cervical cells, cervical adenocarcinoma tissue, and an adenocarcinoma cell line (SiSo)," *Gynecol. Oncol.* 85(1), 170-174 (2002)

99. H. Mantsch and R.N. McElhaney, "Application of IR spectroscopy to biology and medicine," *J. Mol. Struct.* 217, 347-362 (1990)

100. P.G. Andrus and R.D. Strickland, "Cancer grading by Fourier transform infrared spectroscopy," *Biospectroscopy* 4(1), 37-46 (1998)

101. M. Diem, S. Boydston-White and L. Chiriboga, "Infrared Spectrocopy of Cells and Tissues: Shining Light onto a Novel Subject," *Appl. Spectrocopy* 53(4), 148A-161A (1999)

102. H. Fabian, M. Jackson, L. Murphy, P.H. Watson, I. Fichtner and H.H. Mantsch, "A comparative infrared spectroscopic study of human breast tumors and breast tumour cell xenografts", *Biospectroscopy* 1(1), 37-45 (1995)

103. C.M. Krishna, G.D. Sockalingum, R.A. Bhat, L. Venteo, P. Kushtagi, M. Pluot and M. Manfait, "FTIR and Raman microspectroscopy of normal, benign, and malignant formalin-fixed ovarian tissues," *Anal. Bioanal. Chem.* 387(5), 1649-56 (2007)

104. R. Mehrotra, A. Gupta, A. Kaushik, N. Prakash and H. Kandpal, "Infrared spectroscopic analysis of tumor pathology," *Indian J. Exp. Biol.* 45(1),71-76 (2007)

105. B.R. Wood, L. Chiriboga, H. Yee, M.A. Quinn, D. McNaughton and M. Diem, 'Fourier transform infrared (FTIR) spectral mapping of the cervical transformation zone, and dysplastic squamous epithelium' *Gynecol. Oncol.* 93(1), 59-68 (2004)

106. C.M. Krishna, G.D. Sockalingum, B.M. Vadhiraja, K. Maheedhar, A.C. Rao, L. Rao, L. Venteo, M. Pluot, D.J. Fernandes, M.S. Vidyasagar, V.B. Kartha and M. Manfait, "Vibrational spectroscopy studies of formalin-fixed cervix tissues," *Biopolymers* 85(3), 214-21(2007)

107. R.K. Sahu, S. Argov, A. Salman, M. Huleihel, N. Grossman, Z. Hammody, J. Kapelushnik and S. Mordechai "Characteristic absorbance of nucleic acids in the Mid-IR region as possible common biomarkers for diagnosis of malignancy," *Technol. Cancer Res. Treat.* 3(6), 629-38 (2004)

108. Alliance for Cervical Cancer Prevention, "Cervical Cancer Prevention Fact sheet," 11 November 2007 <www.path.org/files/RH_pap_smears.pdf>

109. G.M. Palmer, C. Zhu, T.M. Breslin, F. Xu, K.W. Gilchrist and N. Ramanujam, "Comparison of multiexcitation fluorescence and diffuse reflectance spectroscopy for the diagnosis of breast cancer," *IEEE Trans Biomed Eng* 50(11), 1233-1242 (2003)

110. W Lin, X. Yuan, P. Yuen, W.I. Wei, J. Sham, P. Shi and J. Qu, "Classification of in vivo autofluorescence spectra using support vector machines," *J. Biomed Opt.* 9(1), 180-186 (2004)

111. P. Diagaradjane, M.A. Yaseen, J. Yu, M.S. Wong and B. Anvari, "Autofluorescence characterization for the early diagnosis of neoplastic changes in DMBA/TPA-induced mouse skin carcinogenesis," *Lasers Surg. Med.* 37(5), 382-395 (2005)

112. C.Y. Wang, C.T. Chen, C.P. Chiang, S.T. Young, S.N. Chow and H.K. Chiang, "Partial least-squares discriminant analysis on autofluorescence spectra of oral carcinogenesis," *Appl. Spectrosc.* 52(9), 1190–1196 (1998)

113. C.Y. Wang, T. Tsai, H.M. Chen, C.T. Chen and C.P. Chiang, "PLS-ANN based classification model for oral submucous fibrosis and oral carcinogenesis," *Lasers Surg. Med.* 32(4), 318-326 (2003)

114. T. Gao, J. Feng and C. Yunxiang, 'Human breast carcinoma tissues display distinctive FTIR spectra: implication for the histological characterization of

carcinomas," *Anal. Cell. Path.* 18, 87-93 (1999)

115. M. Jackson, L.P. Choo, P.H.Watson, W.C. Halliday and H.H. Mantsch, "Beware of connective tissue proteins: assignments and implications of collagen absorption in infrared spectra of human tissues," *Biochem. Biophysic. Acta.* 1270(1), 1-6 (1995)

116. B. Bird, M. Miljkovic, M. Romeo, J. Smith, N. Stone, M. George and M. Diem, "Infrared micro-spectral imaging: distinction of tissue types in axillary lymph node histology," *BMC Clin. Path.* 8:8 (2008)

117. R.W. Waynanat, I.K. Ilev and I. Gannot, "Mid-infrared laser applications in medicine and biology" *phil. trans. of the royal society* 359(1780), 635-644 (2001)

118. P. Lasch, W. Haensch, D. Naumann and M. Diem, "Imaging of colorectal adenocarcinoma using FT-IR microspectroscopy and cluster analysis," *Biochim Biophys Acta Mol Basis Dis* 1688, 176-186 (2004)

119. P. Lasch, W. Wasche, W.J. McCarthy, G. Muller and D. Naumann, "Imaging of human colon carcinoma thin sections by FTIR microspectrometry," *Proc. of SPIE* 3257(3),187-197(1998)

120. C. Paluszkiewicz and W.M Kwiatek, "Analysis of human cancer prostate tissues using FTIR microspectroscopy and SRIXE techniques," *Journal of Molecular Structure* (565-566), 329-334 (2001)

121. T. Richter, G. Steiner, M.H. Abu-Id, R. Salzer, R Bergman, H. Rodign and B. Johannsen, "Identification of tumor tissue by FTIR spectroscopy in combination with positron emission tomography," *Vibrational Spectroscopy* (28)1, 103-110 (2002)

122. M.A. Mackanos and C.H. Contag, "FTIR microspectroscopy for improved prostate cancer diagnosis," *Trends in Biotechnology* 27(12), 661-663 (2009)

123. C. Krafft, D. Codrich, G. Pelizzo and V. Sergo, "Raman and FTIR imaging of lung tissue: Methodology for control samples," *Vibrational Spectroscopy* (46)2, 141-149 (2008)

124. C.S. Coley, J.C. Hebden, D.T. Delpy, A.D. Cambrey, R.A. Brown, E.A. Zibik, W.H. Ng, L.R. Wilson and J.W. Cockburn, "Mid-infrared optical coherence tomography," *Rev. of Sci. Instruments* (2007)

125. B.Guo, Y. Wang, C. Peng, H.L Zhang, G.P. Luo, H.Q. Le, C. Gmachl, D.L. Sivco, M.L. Peabody and A.Y. Cho, "Laser-based mid-infrared reflectance imaging of biological tissues," *Optics Express* 12(1), 208-219 (2004)

126. B. Guo, Y. Wang, C. Peng, G.P. Luo and H.Q. Le, "Multi-Wavelength Mid-Infrared Micro-Spectral Imaging using Semiconductor Lasers," *Applied Spectroscopy* 57(7), 811-822 (2003)

127. C.A. Michaels, "Mid-infrared imaging with a solid immersion and broadband laser source," *Appl. Phys. Letters* 90, 121131 (2007)

128. B. Appiah, V. Nammalvar and R. Drezek, "Mid-IR imaging system for breast cancer," MIRTHE workshop, Baltimore MD (2008)

129. P.T. Wong, R.K. Wong and B. Rigas, "Infrared spectroscopy of exfoliated human cervical cells: evidence of extensive structural changes during carcinogenesis," *Proceedings of the National Academy of Science* 88(24), 10988-92 (1999)

130. L. Chiriboga, P. Xie, H. Yee, V. Vigorita, D. Zarou, D. Zakim and M. Diem, "Infrared Spectroscopy of Human Tissue. I. Differentiation and Maturation of Epithelial Cells in the Human Cervix," *Biospectroscopy* 4, 47-53 (1998)

131. R. Mendelsohn, P. Eleftherios, and A. Boskey, "Infrared spectroscopy, microscopy, and microscopic imaging of mineralizing tissue: spectra-structure correlations from human iliac crest biopsies" *Journal of Biomedical Optics* 4(1), 14-21 (1999)

132. T.T. Wong, R. Wong and M. Fung, "Pressure-Tuning FT-IR Study of Human Cervical Tissues," *Applied Spectroscopy* 47(7), 1058-1063 (1993)

133. B. Rigas, S. Morgello and P.T. Wong, "Infrared spectroscopy of exfoliated human cervical cells: evidence of extensive structural changes during carcinogenesis," *PNAS* 88(24), 10988-92 (1999)

134. TE Tech, 10 September 2010 http://www.tetech.com/docs/

135. C. Petibois, G. Cazorla, and G. Déléris, "Triglycerides and Glycerol Concentration Determinations Using Plasma FT-IR Spectra," *Appl. Spectrosc.* 56, 10-16 (2002)

136. B. Mizaikoff, "Mid-IR Fiber-Optic Sensors," *Analytical Chemistry* 75 (11), 258A-267A (2003)

137. U. Bindig, M. Meinke, I. Gersonde, O. Spector, I. Vasserman, A. Katzir, and G. Müller, "IR-biosensor: flat silverhalide fiber for bio-medical sensing?," *Sens. Actuators B Chem.* 74(1-3), 37–46 (2001)

138. M. A. Mackanos, J. Hargrove, R. Wolters, C. B. Du, S. Friedland, R. M. Soetikno, C. H. Contag, M. R. Arroyo, J. M. Crawford and T. D. Wang, "Use of an

endoscope-compatible probe to detect colonic dysplasia with Fourier transform infrared spectroscopy," *J. Biomed. Opt.* 14(4), 044006 (2009)

139. M. A. Mackanos and C. H. Contag, "Fiber-optic probes enable cancer detection with FTIR spectroscopy," *Trends in biotechnology* 28(6), 317-323 (2010)

140. R.K. Sahu and S. Mordechai, "Fourier transform infrared spectroscopy in cancer detection," *Future Onco.* 1(5), 635-647(2005)

141. V.K. Katukuri, J. Hargrove, S.J. Miller, K. Rahal, J.Y. Kao, R. Wolters, E.M. Zimmerman and T.D Wang, "Detection of colonic inflammation with Fourier transform infrared spectroscopy using a flexible silver halide fiber," *Biomedical Optics Express* (1)3, 1014-1025 (2010)

142. H. S. Cooper, L. Everley, W. C. Chang, G. Pfeiffer, B. Lee, S. Murthy, and M. L. Clapper, "The role of mutant Apc in the development of dysplasia and cancer in the mouse model of dextran sulfate sodium-induced colitis," *Gastroenterology* 121(6), 1407–1416 (2001)

143. Q. B. Li, Z. Xu, N. W. Zhang, L. Zhang, F. Wang, L. M. Yang, J. S. Wang, S. Zhou, Y. F. Zhang, X. S. Zhou, J.S. Shi and J. G. Wu, "In vivo and in situ detection of colorectal cancer using Fourier transform infrared spectroscopy," *World J. Gastroenterol.* 11(3), 327–330 (2005)

144. M.G. Muller, I. Georgakoudi and M.S. Feld "Diagnosing invisible cancer with tri-modal spectroscopy," In Proceedings of the XV International Conference on Laser 264-272 (2001)